Thesis for the Degree of Ph. D.

Development of a Novel Technique for Radon Detection Based on Liquid Scintillation Counting System

Department of Physics, Major in Nuclear Physics
The Graduate School

Amos Vincent Ntarisa

June 2022

The Graduate School
Kyungpook National University

Development of a Novel Technique for Radon Detection Based on Liquid Scintillation Counting System

Amos Vincent Ntarisa

Department of Physics, Major in Nuclear Physics
The Graduate School

Supervised by Professor HongJoo Kim

Approved as a qualified thesis of Amos Vincent Ntarisa
for the degree of Ph.D. by the Evaluation Committee

June 2022

Chairman Guinyum Kim ㊞

MooHyun Lee ㊞

Sunghwan Kim ㊞

Jik Lee ㊞

HongJoo Kim ㊞

The Graduate School council
Kyungpook National University

Table of Contents

List of Figures

List of Tables

Development of a Novel Technique for Radon Detection Based on Liquid Scintillation Counting System*

Amos Vincent Ntarisa

Department of Physics, Major in Nuclear Physics
The Graduate School, Kyungpook National University,
Daegu, Korea
(Supervised by Professor HongJoo Kim)

Abstract

Radon detection and measurement are becoming more popular due to their detrimental impacts on human health. Radon is the second leading cause of lung cancer after cigarette smoking and, in general, is the leading cause of lung cancer in people who have never smoked in their lives. The present study used a novel liquid scintillation technique to detect three naturally occurring radon isotopes (^{222}Rn, ^{220}Rn, and ^{219}Rn) concurrently. The detection method uses the delayed coincidence technique as well as pulse shape discrimination, which is accomplished using digital charge comparison. Additionally, Monte Carlo simulations were used to determine the detector's gamma response functions using standard ^{22}Na, ^{60}Co, and ^{137}Cs gamma sources. Furthermore, by comparing the measured and simulated light output distributions, the detector resolution and energy calibration parameters were also determined.

* A thesis submitted to the Council of the Graduate School of Kyungpook National University in partial fulfillment of the requirements for the degree of Ph.D. in June 2022.

Before the measurements were carried out, radon gas from the atmosphere was infused into 700 mL of Ultima Gold AB for 48 hours. The minimum detectable activities of ^{222}Rn (^{238}U),^{220}Rn (^{232}Th), and ^{219}Rn (^{235}U) decay chains were determined to be 1.7, 1.0, and 1.2 mBq/L, respectively. The novel technique proposed in this study has the potential to be used to identify all three naturally occurring radon isotopes in water samples.

Chapter 1. Introduction

1.1 Background radiation

Radiation is energy that is in motion, either as waves or as streams of particles. Radiation can be classified as either ionizing or non-ionizing radiation. Ionizing radiation has the power to dislodge electrons from their orbits around atoms, disrupting the electron or proton balance and potentially causing cell damage. Examples of ionizing radiation include neutron, alpha, and beta particles, as well as gamma and x-rays. Examples of non-ionizing radiation are visible light, sound, ultraviolet, infrared, radio, and television signals [1]. Figure 1.1 shows the electromagnetic spectrum for both ionizing and non-ionizing radiation.

We are surrounded by background radiation. Some of it originates from natural sources, while others are man-made artificial sources. Examples of natural background radiation sources are terrestrial, cosmic, and internal radiation. On the other hand, man-made sources include radiation therapy, diagnostic X-rays, tobacco, televisions, nuclear medicine, etc. Figure 1.2 shows the natural and man-made radiation sources. In the following three subsections of this part, terrestrial, cosmic, and internal radiation will be discussed in brief.

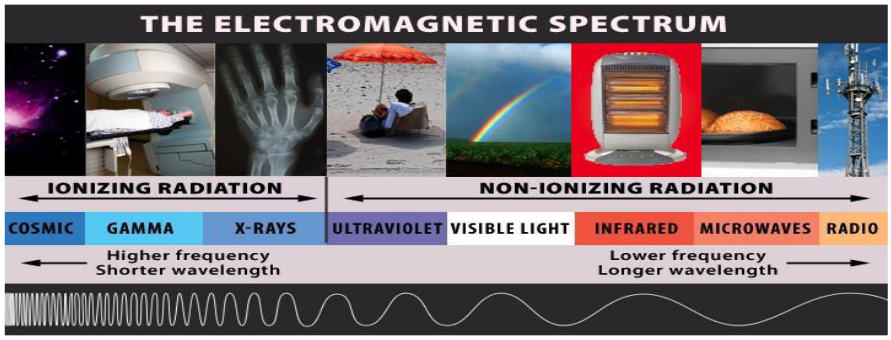

Figure 1.1: The electromagnetic spectrum [1].

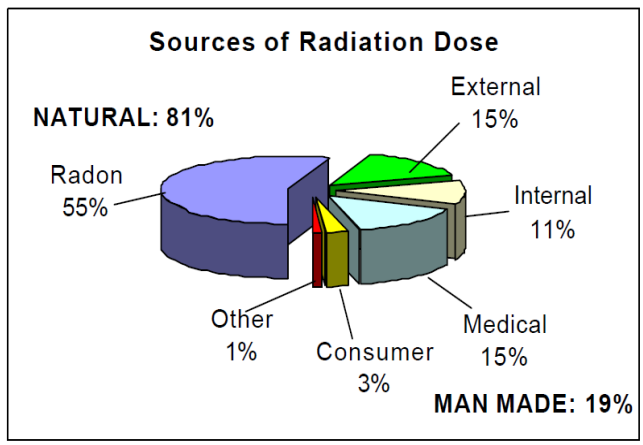

Figure 1.2: Natural and man-made radiation sources [2]

1.1.1 Terrestrial radiation

Many radioactive isotopes have been present since the world was created. All of the shorter-lived radionuclides have decayed since then. Only radionuclides with extremely long half-lives, as well as their decay products, remain. These naturally occurring radionuclides with extremely long half-lives include uranium and thorium isotopes and their decay products like radon. Therefore, these radionuclides cause external exposure to gamma rays and exposure from inhaling radon and its daughters [2,3]. The primary sources of these radionuclides are water, soil, rocks, building materials, etc.

1.1.2 Cosmic radiation

Cosmic radiation is a type of radiation that comes from space and hits the earth all the time. A stream of cosmic radiation comes from the sun, others from stars in the galaxy, etc. Cosmic ray particles collide with Earth's upper atmosphere, causing showers of lower-energy particles. The atmosphere absorbs many of these lower-energy particles. However, others escape. Cosmic radiation at sea level is mostly made up of muons, neutrons, electrons, and gamma-rays. Individuals are more exposed to cosmic rays at higher elevations than at sea level. The cosmic radiation dose rises with altitude, double approximately every 6,000 feet [2].

1.1.3 Internal radiation

Radioactive materials that come from nature are found in the human body. It is primarily from naturally occurring radioactive nuclides in our food and the air we breathe. The primary isotope is potassium-40 (^{40}K). It is because potassium has been present naturally in the human body since birth, and we continue to eat foods that contain potassium. Other isotopes that are present in the human body are tritium (^{3}H), carbon-14 (^{14}C), etc [2]. Tables 1.1 and 1.2 show the annual effective natural and artificial background radiation doses worldwide in millisievert (mSv) [3].

Table 1.1: The annual effective natural background radiation doses worldwide in mSv[3].

Source	Dose range	Worldwide average
Inhalation of ^{222}Rn	0.2-10	1.26
Cosmic rays	0.3-1	0.39
Terrestrial gamma rays	0.3-1	0.48
Ingestion (^{40}K)	0.2-1	0.29
Total	**1-13**	**2.4**

Table 1.2: Annual effective radiation doses of artificial sources worldwide in mSv[3].

Source	Dose range	Worldwide average
Medical diagnosis	Zero-several tens	0.6
Atmospheric nuclear test	Some higher doses around test sites still occur	0.005
Occupational exposure	0-20	0.005
Chernobyl accident	In 1986 the average dose to >300,000 recovery workers ~150 and 350,000 other individuals received doses > 10	0.002
Nuclear fuel cycle (Public exposure)	Up to 0.02 for critical groups at 1km from some nuclear reactor sites	0.0002
Total	**Zero-several tens**	**0.6**

1.2 Radon

The naturally occurring radon isotopes are formed as the result of the natural radioactive decay chains of uranium (^{238}U and ^{235}U) and thorium (^{232}Th). There are three naturally occurring radon isotopes which are ^{222}Rn (radon), ^{220}Rn (thoron), and ^{219}Rn (actinon), with their half-life ($T_{1/2}$) of 3.8 days, 56 s and 4 s, respectively. They are produced by alpha decay from their radium parents ^{226}Ra ($T_{1/2}$ =1600 years), ^{224}Ra ($T_{1/2}$ = 3.63 days), and ^{223}Ra ($T_{1/2}$ =11.4 days), respectively. Their radium parents are produced from the natural decay of ^{238}U ($T_{1/2}$ =4.47 billion years), ^{232}Th ($T_{1/2}$ =14.05 billion years), and ^{235}U ($T_{1/2}$ =703.8 million years), respectively, in most soils, rocks, and water all over the earth [4–8]. Figure 1.3 shows decay series of ^{238}U, ^{232}Th, and ^{235}U, which decay to stable lead ^{206}Pb, ^{208}Pb, and ^{207}Pb, respectively, after several decay chains.

In recent years many researchers have devoted great attention to the evaluation of the effects produced by naturally occurring radioactivity and how to minimize the impact on the people. Most attention has been paid to radon, particularly to the problems of radon exposure to humans. It is due to the fact that radon is the most significant natural source of radiation in the environment at about 55 % [2,9,10]. Radon is the second leading cause of lung cancer after cigarette smoking and, in general, is the leading cause of lung cancer in people who have never smoked in their lives [11–17]. The organizations such as the World Health Organization (WHO), the International Agency for Research on Cancer (IARC), and the United States Environmental Protection Agency (US EPA) all have recognized radon as a human carcinogen [13,14,16,18–20].

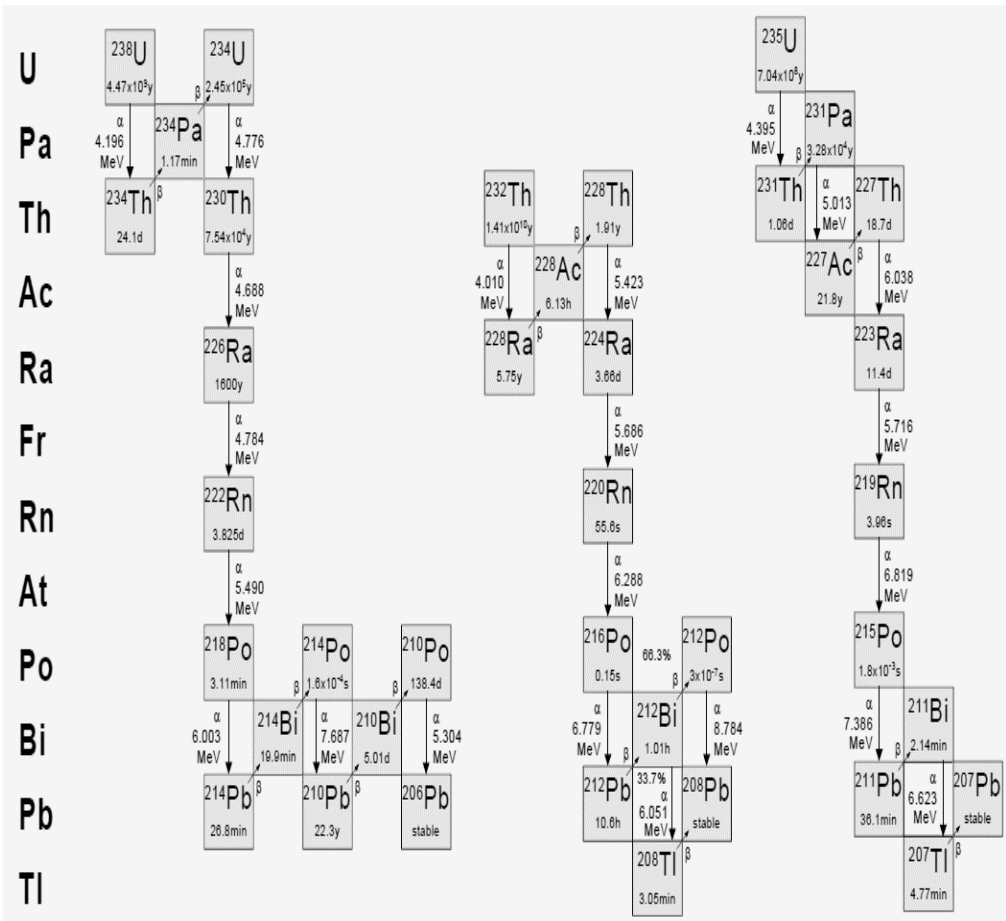

Figure 1.3: The decay series of ^{238}U, ^{232}Th, and ^{235}U [21].

The radon isotope ^{222}Rn has gained more interest due to its longer half-life and greater abundance than the other two naturally occurring radon isotopes. Based on their half-lives, only the radon isotopes ^{222}Rn and ^{220}Rn are predicted to produce large doses in the event of ingestion. Therefore, ^{219}Rn and its progeny are often not considered a health hazard in the workplace because it is generally low, and their presence can be ignored [22,23]. But there are several conditions in which the doses resulting from inhaling ^{219}Rn

and its daughters need to be considered. For instance, in 1980, radiological examinations of historic uranium ore processing plants found elevated amounts of airborne ^{219}Rn progeny. [23]. Therefore, all of these isotopes will have adverse effects on human beings [11–16,18–20,24,25].

1.3 Uranium exploration and mining activities in Tanzania

Tanzania is a mining country that produces metals (such as gold, iron ore, nickel, copper, cobalt, and silver), industrial minerals (such as tanzanite, diamonds, ruby, salt, phosphate, and graphite), and fuel minerals (coal and uranium). Tanzania is the only country in the world that produces Tanzanites. Tanzania also has a large number of rare earth and critical minerals that are currently being explored [26]. Uranium exploration encompasses a variety of actions aimed at determining whether or not there is uranium under the ground. Uranium exploration may include mapping, surveying the ground, evaluating water and soil samples, public awareness, capacity building, and drilling. If the exploration process identifies uranium that can be mined commercially, mining may become feasible in the future [27–30].

In Tanzania, following several radiometric survey researches conducted, the uranium exploration map was identified in the 1970s [31,32]. The places such as Namtumbo (Mkuju river), Bahi, Manyoni, Galapo, Minjingu, Mbulu, Simanjiro, Lake Natron, Tunduru, Songea, Madaba, and Nachingwea have all discovered significant uranium deposits. The Mkuju river project, located in southern Tanzania about 470 kilometers southwest of Dar es Salaam, is one of the major uranium development projects. The mineral resource base of this project represents approximately 58,500 tons of uranium [33]. Figure 1.4 shows the total discovered phosphate and uranium in Tanzania

by 2017 [34]. Block A represents Mkuju and Madaba while block B is the area of Isuna, Bahi and Makutupora. Block C represents Ndala, Igombe, Kigoma, Ugalla river, and Mpanda. Additionally, block D is the area of Minjingu and Gallapo, while block E is Monduli and Tarosero. Lastly, block F represents Chimala, Panda, and Njombe, while block G represents Bukoba and Biharamulo [34].

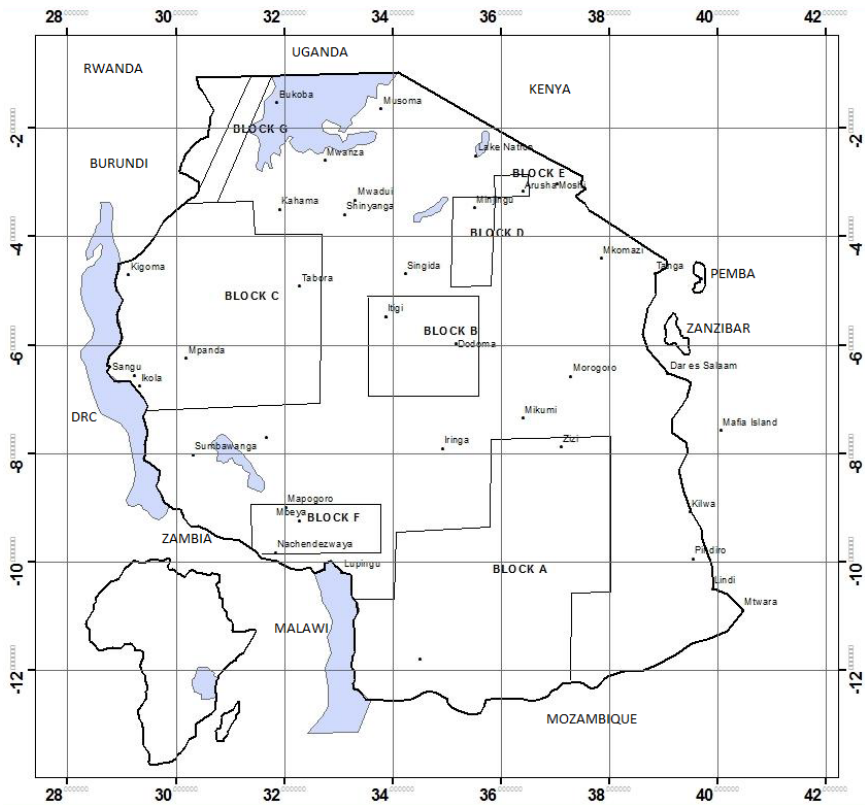

Figure 1.4: The Tanzanian map shows the discovered phosphate deposits (dots) and uranium (blocks). The inset shows the position on the African continent [34].

However, there are several challenges to encounter during uranium explorations. Some of them are regulatory framework, wildlife conservation

issues, public acceptance, and uranium spot price [32]. For example, the Uranium exploration projects were stopped immediately when the global uranium price fell in the market by 2013, and the price dropped to more than 25% in 2016 [32]. However, Gladiator Resources Ltd (ASX: GLA) recently announced on March 28, 2022, to continue exploring different sites in Tanzania [35]. Figure 1.5 shows the Gladiator project locations in Tanzania. We may see other investments in new and old uranium exploration projects start and continue in the future.

Figure 1.5: The Gladiator Project locations in Tanzania [35].

1.4 The motivation for the study

There are several methods and techniques developed in the last few years by researchers and scientists for radon detection and measurements due to the effect of radon on people, especially radon isotope (^{222}Rn). Some of them are the Lucas cells, AlphaGUARD monitor, the ionization chamber, gamma-ray spectrometry, alpha-track detectors, and liquid scintillation counting (LSC) [36–39]. Compared to other methods and techniques, LSC has many advantages, as explained in literature [36,40–43]. High counting efficiency for alpha particles that approaches 100%, simple sample preparation, and a low detection limit are just a few of the benefits. Most of the developed techniques were developed to detect ^{222}Rn only. In the literature, however, no techniques can concurrently detect all three naturally occurring radon isotopes (^{222}Rn, ^{220}Rn, and ^{219}Rn). Thus, it motivated me to develop a novel technique for radon detection based on an LSC system that can detect all three naturally occurring radon isotopes. The detection system employs the neutron tagging module (NGT400), which tags neutron signals from a liquid scintillator and photomultiplier tube (PMT) by using the delayed coincidence technique (DCT) and the pulse shape discrimination (PSD), which is implemented by digital charge comparison (DCC) method. Additionally, an Ultima Gold AB (alpha/beta discrimination) (UG-AB) organic liquid scintillation cocktail is used in this technique. Using DCT in this technique makes it easy to reduce background radiations which is an added advantage compared to other techniques. Therefore, the proposed technique has the significant benefit of simultaneously detecting all three naturally occurring radon isotopes with relatively high efficiency and low detection limit compared to many other developed techniques based on LSC.

In comparison to previously developed techniques, which are based on detecting only ^{222}Rn, the proposed novel technique can be utilized to detect all three naturally occurring radon isotopes in water more efficiently. In Tanzania, there are many places found with a relatively high abundance of uranium deposits. Therefore, the developed novel technique can be well used to detect all three naturally occurring radon isotopes (^{222}Rn, ^{220}Rn, and ^{219}Rn) in water samples from different places around Tanzania for the health of the people in the vicinity of uranium deposits. Radon levels are particularly high in areas where the water, soil, or rock contains a high uranium concentration. Given that radon is one of the reliable indicators of uranium availability in an area, it can also be utilized for other purposes, such as searching for new uranium deposits. As a result, the people who live in or near these locations should have their health taken into consideration by the government of Tanzania.

1.5 Organization of the thesis

This thesis focuses on the development of a novel technique for radon detection based on a liquid scintillation counting system. Besides this chapter, there are five more chapters. Chapter 2 is about the theoretical background, in which the interactions of gamma rays with matters and the mechanism in liquid scintillation are explained. Chapter 3 deals with experimental setup, experimental arrangements, and data acquisition system. Chapter four deals with data analysis procedures. Chapter 5 presents results and discussions. Finally, chapter 6 is the summary and conclusion.

Chapter 2. Theoretical background

2.1 Interaction of gamma rays with matters

Gamma rays (γ-rays) interact with matters in three major processes: the photoelectric effect, Compton effect, and pair production [44–46]. The following three subsections will be dedicated to a short explanation of these processes.

2.1.1 Photoelectric effect

An incident photon transfers its energy to an orbital electron, causing the electron to be ejected from the atom via the photoelectric process. The ejected electron is called a photoelectron and will leave a vacancy which will be filled by a free electron or outer shell electron. This photoelectron will have kinetic energy (E_e) given by the relation of equation 2.1.

$$E_e = hv - E_b, \tag{2.1}$$

where h is the Planck's constant and v is the photon frequency. This process will happen only when the incident photon energy (hv) is greater than the binding energy (E_b). The most likely source of the photoelectron is the atoms which are more tightly bonded [46–48]. Figure 2.1 shows the photoelectric effect process. The cross-section indicates the probability of interaction of two particles. The probability for the photoelectric absorption per atom (τ) is described in equation 2.2.

$$\tau = C \times \frac{Z^n}{h\nu^{3.5}} \ , \qquad 2.2$$

where C is a constant, Z is the atomic number, and n is a number between 4 and 5. Therefore, photon absorption is most effective in high Z-materials and high-density materials. The photoelectric effects take place on a few hundred keV.

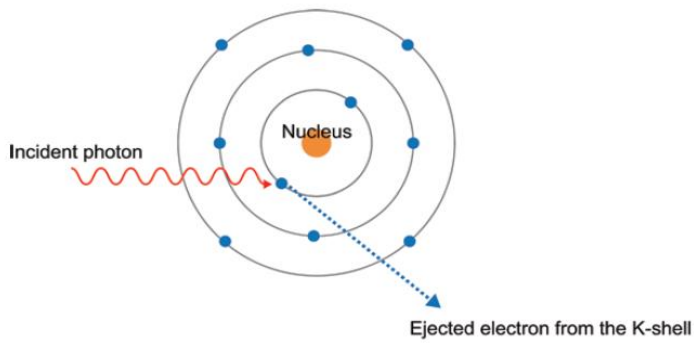

Figure 2.1: The photoelectric effect process [49].

2.1.2 Compton effect

The Compton effect (Compton scattering) involves the interaction between incident γ-ray photon and electron, which is assumed initially to be stationary or free. After the interaction, the incident photon is called a scattered photon deflected through an angle θ from its original direction. The electron is called a recoil electron at an angle ϕ from its rest position. Following this event, a part of the energy carried by the incident γ-ray photon is transferred to the recoil electron, and the scattered photon travels with lower energy. Figure 2.2 shows the Compton effect process.

The energy in the Compton effect can be derived by assuming that the binding of the electron is too small, which means it can be negligible assuming that the incident γ-ray interacts with a free electron [46,48,50]. And also, by taking care of the conservation of energy, momentum, and relativistic relationship, the scattered photon will have energy presented in equation 2.3.

$$hv' = \frac{hv}{1+\frac{hv}{m_e c^2}(1-cos\theta)} \quad , \qquad 2.3$$

where m_e is the mass of the free electron and c is the speed of light. The recoil electron will have its energy (E_{recoil}) expressed in equation 2.4.

$$E_{recoil} = hv - hv' = hv - \frac{hv}{1+\frac{hv}{m_e c^2}(1-cos\theta)} \qquad 2.4$$

The scattered photon can take any angle between 0 to 180^0. When θ = 180^0, the scattered photon will have the minimum energy while the recoil electron will have the maximum energy. If we let $E_\gamma = hv$ (the energy of the incident γ-rays in MeV), substituting the value of θ = 180^0 and $m_e c^2 = 0.511$ MeV in equation 2.4 will result in equation 2.5, which is the maximum energy of Compton edge (E_c) in MeV.

$$E_c = \frac{2{E_\gamma}^2}{0.511+2E_\gamma} \qquad 2.5$$

For example, if 0.662 MeV of the incident γ-rays from ^{137}Cs is put in equation 2.5, we will have the maximum Compton edge energy of 0.477 MeV. With increasing Z, the probability of Compton scattering per atom (σ) also increases. Organic scintillators are usually made of low Z and low-density

materials. Therefore, Compton scattering is the leading cause of the spectra produced in organic liquid scintillators because photoelectric absorption has a low influence in this situation [51–56].

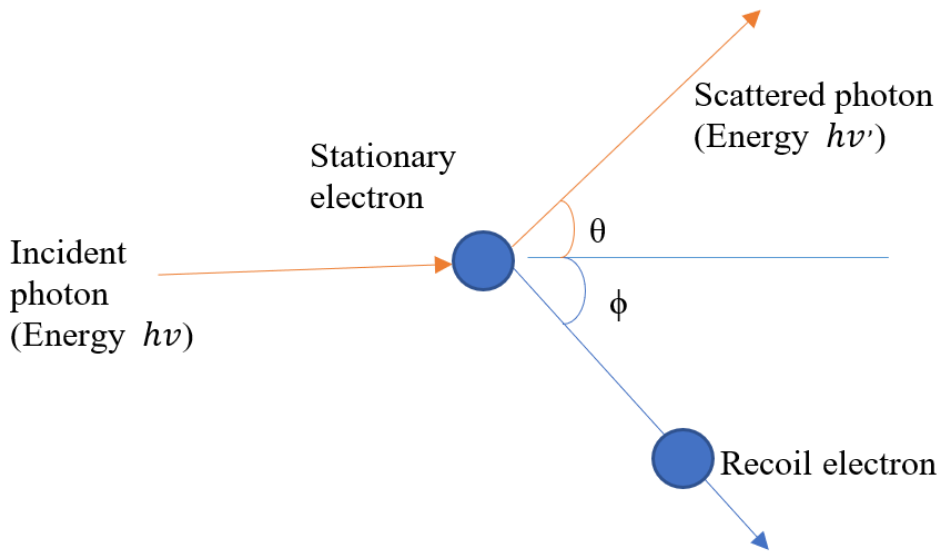

Figure 2.2: The Compton effect process.

2.1.3 Pair production

Pair production occurs when an incident γ-ray photon with energy greater than 1.022 MeV (twice the resting electron) interacts with the nucleus Coulomb field. After the interaction, the incident γ-ray photon completely disappears, and the electron (e^-) and positron (e^+) are produced with the same mass as an electron. Figure 2.3 is a representation of the pair production process. The energy of the electrons-positron produced will be the difference between the energy incident γ-ray photon and 1.022 MeV. Equation 2.6 presents this explanation.

$$E_{e^-} + E_{e^+} = hv - 1.022 \text{ MeV} \quad (2.6)$$

The probability of pair production per nucleus (κ) is directly proportional to Z^2. Figure 2.4 shows the summary of three dominant interactions of γ-rays with matters. The photoelectric effect is dominant in the lower energy region, while the Compton effect is dominant in the middle region, and pair production is dominant in the higher energy [46,57–59].

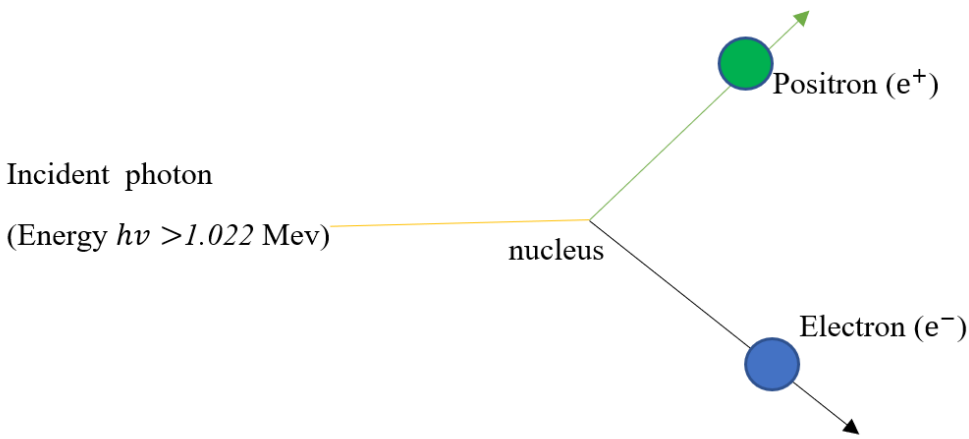

Figure 2.3: Pair production process.

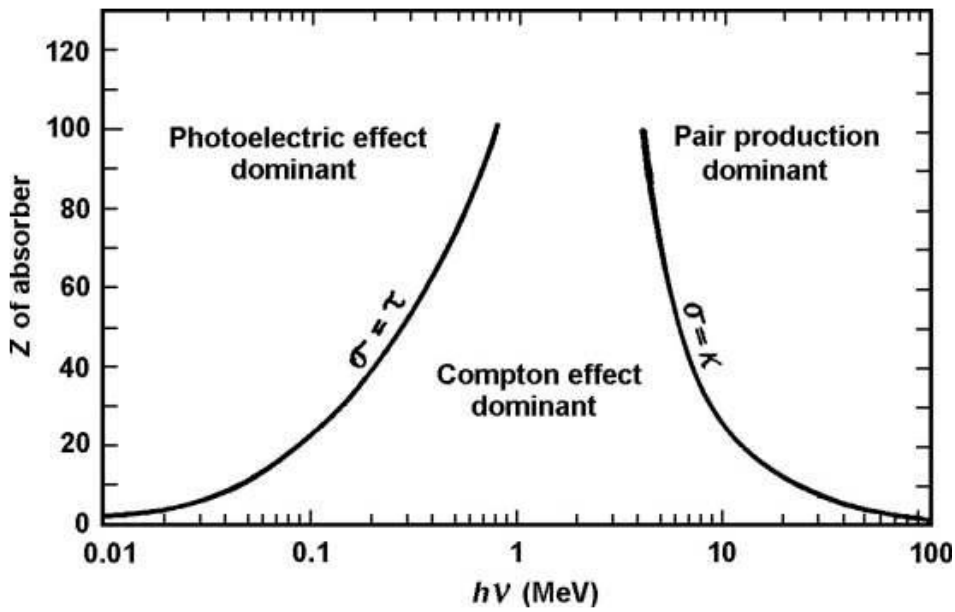

Figure 2.4: Three major dominant interactions of γ-rays with matters [58].

2.2 Scintillation Detectors

In the scintillation detectors, the ionizing radiation passes through a scintillator material, and sparks or scintillations of light are produced as near-visible light. The scintillator produces a very little amount of light. Therefore, it must be amplified by PMT before it can be recorded. Figure 2.5 shows the basic principle of a scintillator detector using PMT. There are three main scintillator materials depending on conditions liquid, solid, and gases. And depending on chemical compositions, there are organic scintillators such as liquid and plastic scintillators and inorganic scintillators like crystals and glasses [46,57,60,61]. A good scintillator for radiation detectors should have a high scintillation efficiency, high optical transparency, short decay time, a high light yield, good energy resolution, and an emission wavelength suitable

for the characteristic of the PMT [57,62–66]. Scintillation detectors have many applications in different fields, such as nuclear and high-energy physics experiments, environmental monitoring, security examination, medical diagnostics, astrophysics experiment, geophysical exploration, and reactor monitoring [46,63,67].

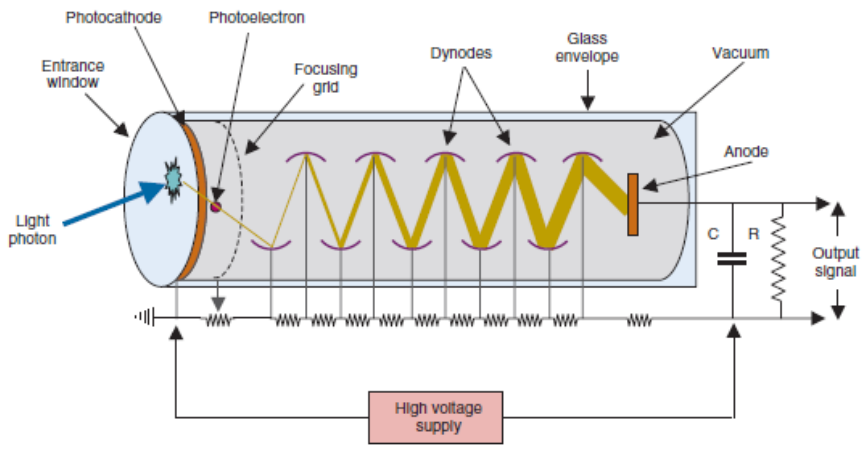

Figure 2.5: The basic principle of a scintillator detector using PMT [61].

2.2.1 Scintillation mechanism in organic scintillators

Organic scintillators are organic materials that emit detectable photons in the visible part of the light spectrum after a charged particle or photon passes through them. Organic materials have a very different scintillation mechanism compared to inorganic materials. Due to the crystal lattice structure, scintillation occurs in inorganic scintillators, such as NaI and CsI. Because fluorescence in organic materials is caused by changes in the energy levels of a single molecule, it can be viewed regardless of its physical state. Generally, practical organic scintillators are organic molecules with

symmetry properties associated with their π −electron structure [46]. Organic scintillators have a decay time of 10^{-8} s, in general, inorganic crystals have slower decay times of about 10^{-6} s. However, inorganic crystals have fast components in their response.

Figure 2.6 shows the energy level diagram of the luminescence mechanism in an organic molecule. This figure shows that the energy from a charged particle is absorbed and excites the electron into a series of excited states. The singlet states (spin = 0) are labeled as S_1, S_2, and S_3, while the triplet (spin 1) are named as T_1, T_2, and T_3, respectively. The energy gap between S_0 and S_1 is typically 3 or 4 eV in organic scintillators, although the energy gap between higher-lying states is slightly smaller. In order to correlate to the molecule's vibrational states, each of these electronic configurations is separated into different levels. The level spacing is typically 0.15 eV. The symbol S_{00} indicates the lowest vibrational level of the ground electronic state. Practically all molecules at room temperature are in the S_{00} state due to the enormous distance between vibrational modes and the average thermal energy (0.025 eV) [46]. When a charged particle passes through, the molecules absorb kinetic energy, then excite electrons to higher levels. The higher singlet electronic states are quickly (picoseconds) de-excited to the S_1 electron state via radiationless internal conversion. Non-thermal equilibrium states like S_{11} and S_{12} quickly lose vibrational energy. As a result of the excitation process, a population of excited molecules in the S_{10} state is formed in a very short time.

In transitions between S_{10} and the ground state, scintillation light, or prompt fluorescence, is emitted. The intensity (I) of prompt fluorescence at time t after excitation is defined by equation 2.7.

$$I = I_0 e^{-t/\tau}, \qquad 2.7$$

where τ is the fluorescence decay time for the S_{10} level. In most organic scintillators, τ is in a few nanoseconds. It means that the prompt scintillation component is very fast. First triplet state T_1 has a longer life than singlet state S_1. Some excited singlet states can be changed into triplet states via an intersystem crossing. T_1's lifetime could be as long as milliseconds. The radiation emitted in a de-excitation from T_1 to S_0 is a delayed light emission defined as phosphorescence. T_1 is below S_0; hence the emitted phosphorescence has a longer wavelength than fluorescent light. Timing and wavelength distinguish phosphorescent light from scintillation light. The length of the upward arrows indicates how intensely photon energy will be absorbed by the material. Because all of the fluorescence transitions represented by downward arrows (except S_{10}-S_{00}) have lower energy than the minimum necessary for excitation, the optical absorption and emission spectra show very little overlap (Stokes shift). As a result, there is little fluorescence self-absorption. Figure 2.7 shows a typical example of an organic scintillator's optical absorption and emission spectra.

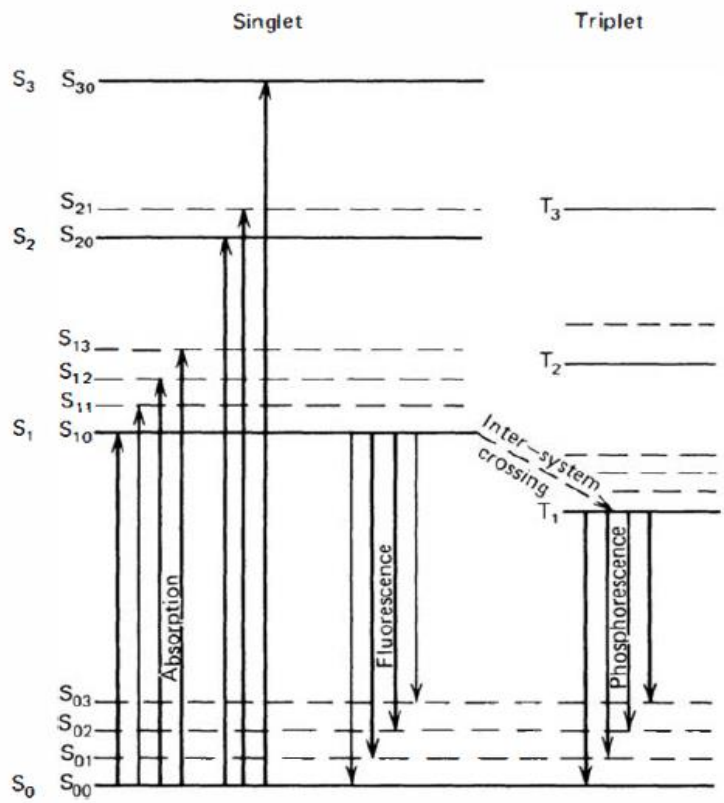

Figure 2.6: The energy level diagram showing the luminescence mechanism in an organic molecule (left is singlet and right is triplet) [46].

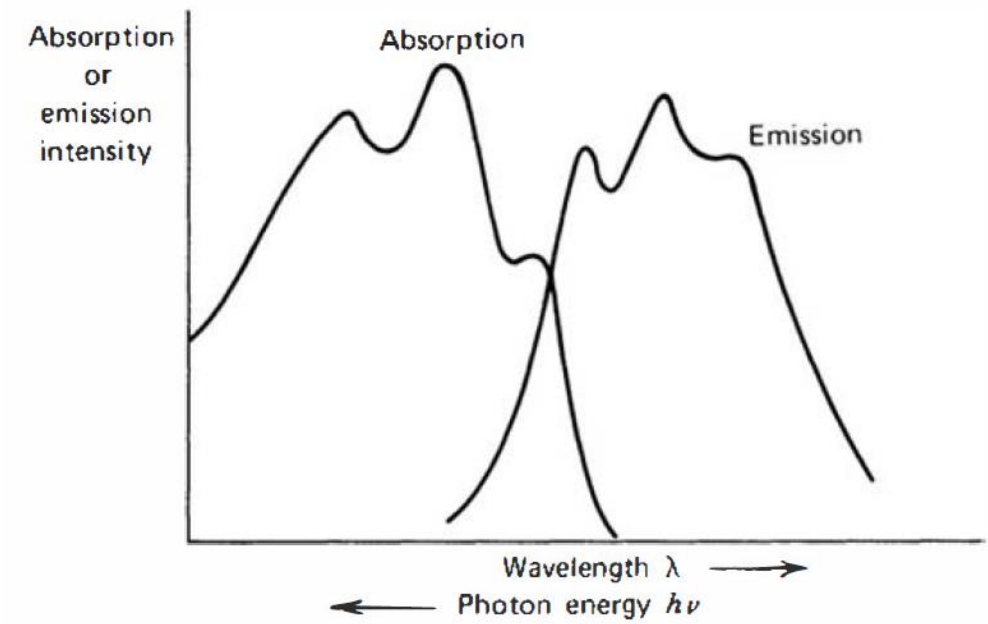

Figure 2.7: A typical example of organic scintillator's optical absorption and emission spectra [46].

2.2.2 Basic theory of pulse shape discrimination (PSD)

PSD is a technique that discriminates between signals emitted by various radiation sources. Typical examples include discrimination between gamma, neutron, and alpha events. Figure 2.8 shows the time dependence of organic scintillation pulses in stilbene gamma-rays, fast neutrons, and alpha-particles. A pulse in an organic scintillator is distinguished by fast (prompt fluorescence) and slow (delayed fluorescence). Compared to the prompt decay time of a few nanoseconds, the slow component has a typical decay time of several hundred nanoseconds. The light fraction in the slow component is determined by the incoming particle, the exciting particle's energy loss rate $\frac{dE}{dX}$ and is the highest for particles with the largest $\frac{dE}{dX}$ [46]. Therefore, heavier

particles like alpha and fast neutrons have higher specific ionization and produce more delayed fluorescence (slow components) light than that produced by gamma-rays. Therefore, PSD can be used to distinguish the mixed events. PSD can be categorized into two main types according to its implementation: either time or frequency domain [68]. In the time domain, samples of the signals are taken at a specific time with regard to peak time and amplitude, making these methods more sensitive to noise and light intensity than other types of methods. In our proposed technique, we used this type of method. Frequency domain approaches are achieved by performing a frequency transform of the digitized pulses, such as the discrete sine transform, the fast Fourier transform, the discrete cosine transform, etc. The following subsection will be dedicated to a brief explanation of PSD by the DCC method. The method used in this study. Other methods for PSD can be found in the literature.

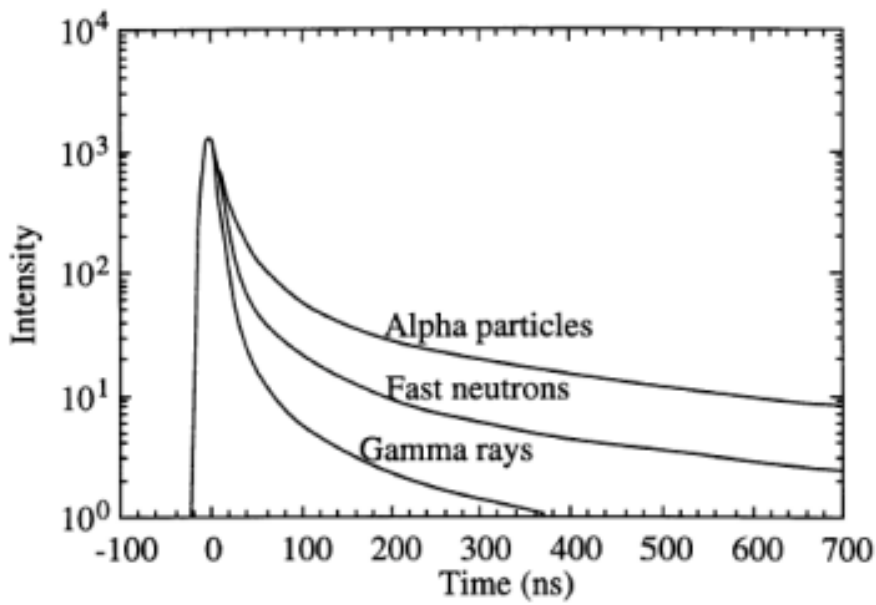

Figure 2.8: The time dependence of organic scintillation pulses in stilbene [69].

2.2.3 PSD by Digital charge comparison (DCC) method

DCC is a preferred method used in PSD. The DCC method's simplicity and effectiveness give the most powerful PSD [70,71]. In most cases, the DCC is used to identify the source of each pulse simply by comparing the tail to the total integral charges. Each pulse of the detecting signal must be integrated across two separate time intervals. Figure 2.9 shows the current pulses associated with gamma-rays and neutrons as a typical example of an organic scintillator using PSD by the DCC method. The cutting time window presented in figure 2.9 is used in this study.

The time signal produced by the gamma-ray interaction is faster than that produced by the neutron interaction [52,72]. The neutron interaction gives a slower timing signal than the gamma-ray interaction. A gamma-ray pulse rises and falls faster from and to the baseline than a neutron pulse generated by recoil protons. The difference between these two is most noticeable in the tail. A neutron generates a large ionization density by generating a recoil proton with a long tail. Gamma rays, on the other hand, produce distributed electrons. It decays much faster as a result of the low ionization density. The main distinction between these two is their pulses in tail parts. So its analysis is based on comparing their tails [72]. Therefore, the PSD parameters are higher for neutrons than for gamma-rays, as shown in figure 2.10. Figure 2.10 shows the n/γ separation from the ^{252}Cf source using a BC-523 liquid scintillator.

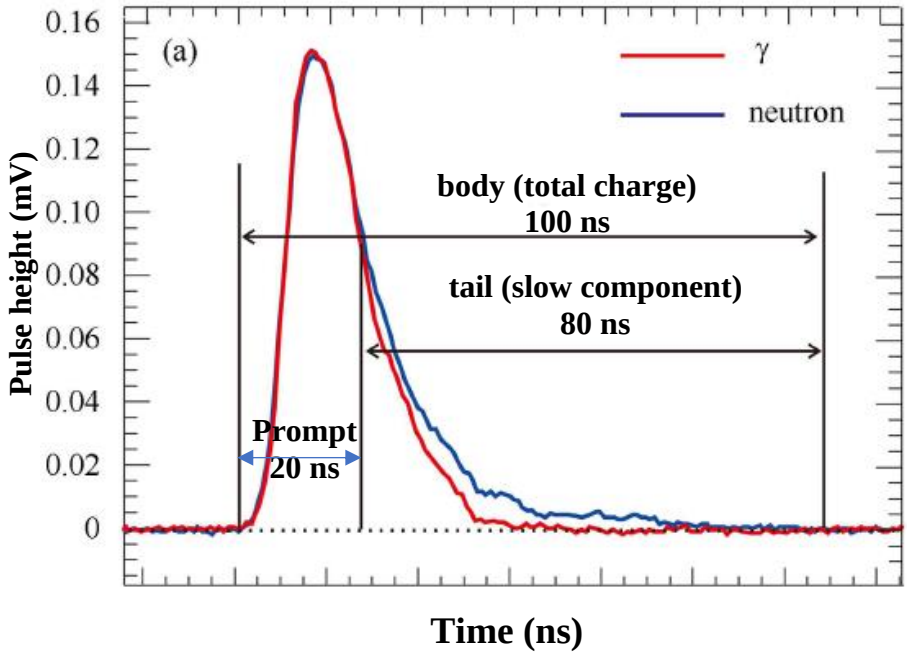

Figure 2.9: The difference between gammas and neutrons in a typical example of an organic scintillator using PSD by the DCC method [73].

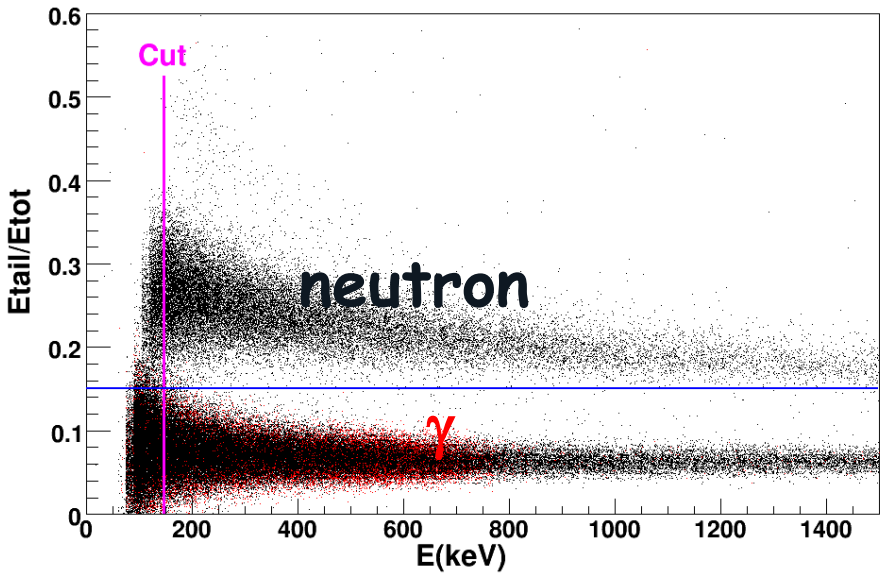

Figure 2.10: The n/γ separation from ^{252}Cf source using BC-523 liquid scintillator [74].

2.2.4 Mechanism in Liquid scintillation counting

The LSC involves mixing the radioactive sample into a scintillation vial and adding a particular scintillation cocktail. The vial can be glass or plastic, and the cocktail is the scintillating liquid. In order to achieve conversion of the energy into a detectable light pulse by a detector, the LSC needs specific cocktails. The cocktail for liquid scintillation contains at least a fluor molecule (scintillator) and an organic solvent molecule [61]. The energy absorbed by the scintillators produces excited states of electrons, which decay to the ground state and gives out a light pulse detected by PMT. Figure 2.11 shows the primary principle mechanism of the LSC system. The following three subsections will be dedicated to the explanation of liquid scintillation cocktails (solvent, scintillator) and quenchers in LSC.

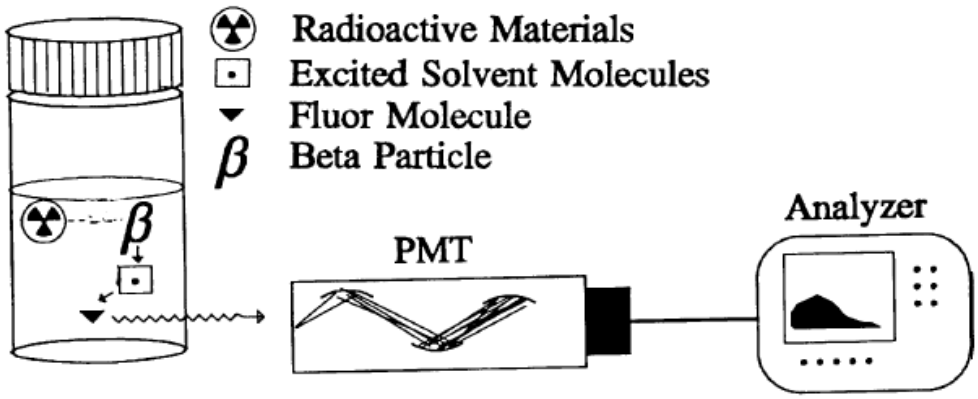

Figure 2.11: The basic principle of the LSC system [75].

2.2.5 Liquid scintillation cocktails

The cocktails for liquid scintillation counting are divided into two main categories: classical and safer cocktails. The cocktails with benzene, xylene, toluene, and pseudocumene are considered classical, while those including phenyl xylyl ethane (PXE), linear alkylbenzene (LAB), and Diisopropylnaphthaline (DIPN) are considered safer [70]. The latter set of cocktails is less hazardous, and no evidence of carcinogenic, mutagenic, or teratogenic behavior has been discovered. Because these cocktails have a much lower vapor pressure, they do not have a strong smell and can be used without fume hoods. The flashpoint of the safer cocktails is substantially higher than room temperature, making laboratory handling much safer. The flashpoint is the lowest temperature at which the gases of a flammable liquid in the air can self-ignite [76]. Considering the advantages of safer cocktails, it is wise to use this type of cocktail in a laboratory. Several safer cocktails are available in the markets, one of which is the Ultima Gold^{TM} family. This family has the additional benefit of having high quench resistance. Among the

member of this family is UG-AB. According to the Perkin Elmer manufacturers' description, the UG-AB was explicitly designed for alpha/beta discrimination in LSC. It has the delayed pulse decay characteristics required for effective alpha/beta discrimination. Therefore, it is specially designed for α/β separation. Its excellent sample holding capacity makes it suitable for a wide range of aqueous and acidic samples [77]. These additional advantages of UG-AB choose to use it, especially dealing with alpha/beta separation. In the absence of UG-AB, the Ultima Gold LLT cocktail can be used alternatively because its ability of α/β separation is not inadequate. In the following subsection of this section, there is a table that shows some availability of commercial liquid scintillation cocktails with some characteristics (Table 2.1).

2.2.6 Solvent, scintillator, and surfactant

Generally, liquid scintillation cocktail mixtures involve four things which are solvent, scintillator, surfactant, and sample. Solvents are used in cocktails for two primary reasons. Before anything else, the sample and the scintillator must be dissolved in a solvent, and it helps the radioisotope transfer energy to the scintillator. Aromatic hydrocarbon compounds are a common group of compounds used as a solvent because of having large conjugated π−electron systems, which are ideal for transferring energy from radionuclides to solvents. Aside from these considerations, the solvent should have a low amount of natural ^{14}C activity and high transmission for photons emitted by the scintillator. The scintillator molecules dissolved in the solvent absorb the energy produced by the solvent and re-emit it as visible light with a wavelength of around 420 nm. Primary and secondary scintillators are the two types of scintillators available. The direct energy transmission between

excited solvent molecules and the scintillator is possible with primary scintillators with the modern PMT. The secondary scintillators were originally utilized as a wavelength shifter to boost PMT sensitivity to a wavelength between 415 and 425 nm. While most modern PMTs can count the light pulses generated by the primary scintillator, secondary scintillators have been discovered to boost efficiency in various situations and are still utilized in most LSC cocktails [78]. The surfactants in a cocktail allow an aqueous sample to come into close contact with the aromatic solvent by forming a stable and clear microemulsion; required for stable conditions during the counting period. Table 2.1 shows LSC cocktails and their characteristics.

Table 2.1: LSC cocktails and their characteristics [76].

Aqueous/ organic samples	**Cocktail**	**solvent**	**Flash point (^{0}C)**	**α/β separation**	**Classical /safer**
	Ultima Gold †	DIPN	~ 150	-	
	Ultima Gold XR	DIPN	~ 150	-	
	Ultima Gold LLT	DIPN	~ 140	Yes	
	Ultima Gold uLLT	DIPN	~ 140	-	
	Ultima Gold MV	DIPN	~ 110	-	
	Ultima Gold AB	**DIPN**	**~ 140**	**Yes (specially)**	
	Ultima-Flo M	PXE/LAB	~ 120	-	
	Ultima-Flo AF	PXE/LAB	~ 120	-	

Cocktails for aqueous and organic samples	Ultima-Flo AP	BT/DPE	~ 120	-	**Safer**
	Opti-Fluor	LAB	~ 150	-	
	Emulsifier-Safe	LAB	~ 150	-	
	Formula 989	LAB	~ 140	-	
	OptiPhase HiSafe II	DIPN	144	-	
	OptiPhase HiSafe III	DIPN	144	-	
	OptiPhase Supermix	DIPN	144		
	LumaSafe	PXE	149	-	
	LumaSafe Plus	PXE	149	-	
	Lumagel Safe	PXE	149	-	
	SafeFluor-S	LAB	149	-	
	Insta-Gel Plus	Pseudocumol	48-50	-	**Classical**
	Pico-Fluor 15(not available)	Pseudocumol	48-50	-	
	Pico-Fluor 40	Pseudocumol	48-50	-	
	Filter-Count	Pseudocumol	48-50	-	
	Hionic-Fluor	Pseudocumol	48-50	-	
	Monophase S	Pseudocumol	48-50	-	
	Permafluor E^+	Pseudocumol	48-50	-	
	Atomlight	Pseudocumol	48-50	-	
	Biofluor	Pseudocumol	48-50	-	
	Aquassure	Pseudocumol	48-50	-	
	Aquasol-2	Xylol	24-26	-	
	Flo Scint II	Pseudocumol	46	-	

	Flo Scint III	Pseudocumol	46	-	
Cocktails for only pure organic samples	Insta-Fluor Plus	Pseudocumol	48-50	-	**Safer**
	Ultima Gold F	DIPN	~ 150	-	
	Opti-Fluor O	LAB	~ 150	-	
	OptiScint HiSafe	DIPN	~ 150	-	
	Insta-Fluor Plus	Pseudocumol	48-50	-	**Classical**
	Econofluor-2	Pseudocumol	48-50	-	
	High Eff. Min. oil Scint.	Pseudocumol	79	-	

Note: Red color represents the cocktail used in this experiment and

- means no available information about α/β separation.

2.2.7 Quench in liquid scintillation counting

The term quench refers to anything that obstructs the scintillation mechanisms and prevents some of the light from being detected by the PMT, resulting in a reduction in the number of counts recorded and a less energy identification [56,79–82]. The two basic types of energy quench may occur in LSC systems: chemical and color quench. Figure 2.12 shows the two main types of quench in LSC systems; chemical quench occurs during energy transfer from solvent molecule to scintillator, and hence the energy will not transfer to the fluor molecule. On the other hand, the color quench happens when the light emitted by the scintillator is absorbed by the color sample. As a result, the signal detected by PMT does not represent the total actual light emitted [82,83]. There are several methods for quench correction. These

methods are balanced quenching, channels ratio, dilution, internal, external standard, extrapolation, and quench curve [61,81,83–85]. The explanation of these methods can be found in the literature [61,84,87].

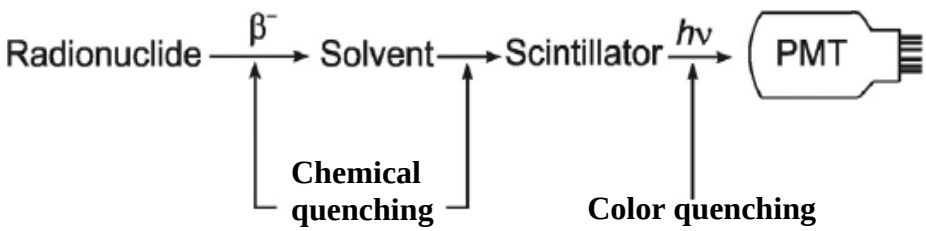

Figure 2.12: The two main types of quenching in LSC systems [87].

2.3 Radioactive equilibrium

Radioactive equilibrium occurs when a radioactive species and its subsequent radioactive products have reached such relative proportions that they all disintegrate at the same numerical rate and keep their proportions constant. If we assume nuclide A decays to nuclide B and B decays to nuclide C, we will have the following relations in equation 2.8.

$$A \xrightarrow{\lambda_A} B \xrightarrow{\lambda_B} C \qquad 2.8$$

The decay constants of radionuclide A and B are denoted by the symbols λ_A and λ_B, respectively. Assuming that the nuclei of each present at the time(t) have the numbers $N_A(t)$ and $N_B(t)$, then the activities are $\lambda_A N_A(t)$ and $\lambda_B N_B(t)$, for each kind of nuclei present at t, respectively. Then the rate of decay of radionuclide B can be written as presented in equation 2.9.

$$\frac{dN_B(t)}{dt} = \lambda_A N_A(t) - \lambda_B N_B(t) \quad 2.9$$

The general solution of this differential equation can be written as in equation 2.10.

$$N_B(t) = \frac{\lambda_A}{\lambda_B - \lambda_A} N_A(0)(e^{-(\lambda_A)t} - e^{-(\lambda_B)t}) + N_B(0)(e^{-(\lambda_B)t}) \quad 2.10$$

We can obtain the activity of radionuclide B as $A_B(t) = \lambda_B N_B(t)$, as presented in equation 2.11.

$$\lambda_B N_B(t) = \lambda_B [\frac{\lambda_A}{\lambda_B - \lambda_A} N_A(0)\left(e^{-(\lambda_A)t} - e^{-(\lambda_B)t}\right) + N_B(0)\left(e^{-(\lambda_B)t}\right)] \quad 2.11$$

If we assume initial conditions $N_A(t = 0) = N_0$ and $N_B(t = 0) = 0$, equation 2.11 can be reduced to equation 2.12.

$$A_B(t) = \frac{\lambda_B}{\lambda_B - \lambda_A} A_A(0)\left(e^{-(\lambda_A)t} - e^{-(\lambda_B)t}\right), \quad 2.12$$

where $A_A(0)$ is the amount of parent radionuclide A present at $t = 0$, other symbols carry their usual meaning as defined before. More details of the derivation of these formulas can be found in other literature [88–91]. Equation 2.12 shows that the rate at which equilibrium is reached is determined by the half-lives of both the parent and daughter nuclides. There are three normal for radioactive equilibrium: secular equilibrium, transient equilibrium, and no equilibrium. The following subsection of this part will be dedicated to a brief explanation of radioactive equilibrium.

2.3.1 Secular equilibrium

Secular equilibrium is possible when the half-life of the parent nuclide is infinitely greater than the half-life of the daughter nuclide. That is $t_A \gg t_B$ or $\lambda_A \ll \lambda_B$. From equation 2.12, we can see that finally, at $t = \infty$ with $(\lambda_B)t = \infty$, the daughter activity reaches a value of activity equal to parent, i.e., $A_B(t) = A_A(t)$. Therefore, as long as a parent isotope decays, the radioactive isotope of the daughter will remain constant. Examples include the relationships between the long-living uranium and thorium isotopes ^{238}U, ^{235}U, and ^{232}Th, and the decay products of their daughter isotopes. For example, the secular equilibrium between the parent ^{226}Ra and daughter ^{222}Rn will start to exist approximately after 7 half-lives of ^{222}Rn, which is about 27 days. In our case, we filled radon from the air in UG-AB container and placed it in a dust-proof environment for 48 hours without closing it, and after that, we started measurement as a sample. After we took a measurement, we waited for ~7 weeks (49 days) without opening the container, and we took a measurement. At this stage, the activities of parent and daughter remain constant. Figure 2.13 shows the secular equilibrium of ^{226}Ra (parent) and ^{222}Rn (daughter).

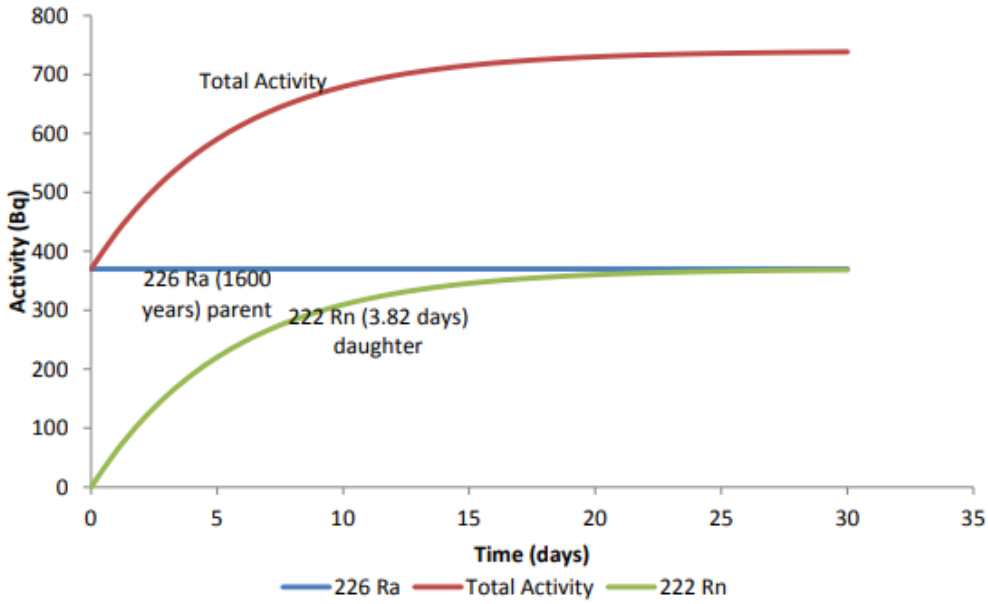

Figure 2.13: The secular equilibrium ^{226}Ra (parent) and ^{222}Rn (daughter) [89].

2.3.2 Transient equilibrium

The transient equilibrium occurs when the parent nuclide has a half-life a few times that of the daughter ($t_A > t_B$ or $\lambda_A < \lambda_B$). The exponential term in equation 2.12 becomes less as time t increases while the activity ratio rises. An example, in this case, includes parent molybdenum-99 (^{99}Mo) with a half-life of 66 h and its daughter Technetium-99m (^{99}Tc) with a half-life of about 6.1 h. Figure 2.14 shows the transient equilibrium between parent (^{99}Mo) and daughter (^{99}Tc).

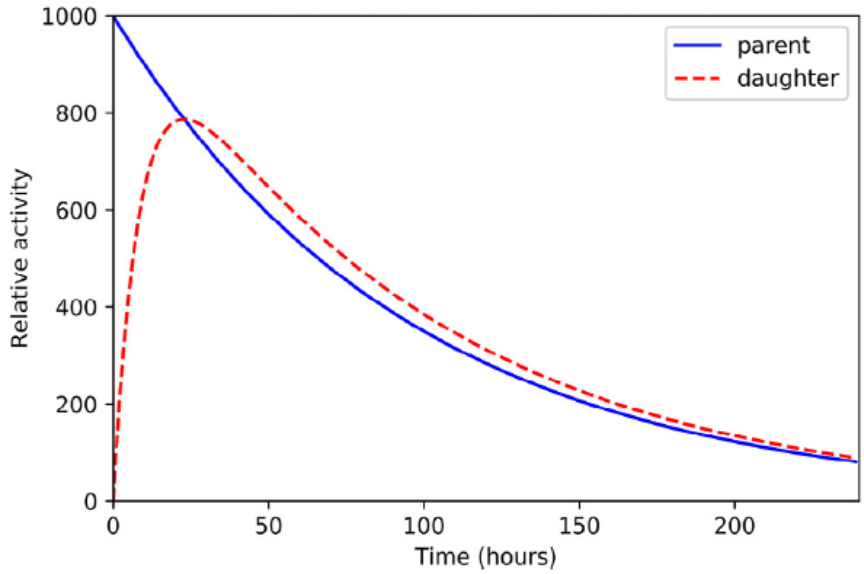

Figure 2.14: The transient equilibrium between ^{99}Mo (parent) and ^{99}Tc (daughter) [92].

2.3.3 No equilibrium

No equilibrium occurs when the parent nuclide has a shorter half-life than the daughter ($t_A < t_B$ or $\lambda_A > \lambda_B$). The daughter's activity achieves a maximum and then decays at its characteristic rate. Meanwhile, the parent decays away due to its lower half-life. The total activity does not reach a maximum in this situation; it diminishes continuously. Figure 2.15 shows no equilibrium between ^{146}Ce (parent) and ^{146}Pr (daughter).

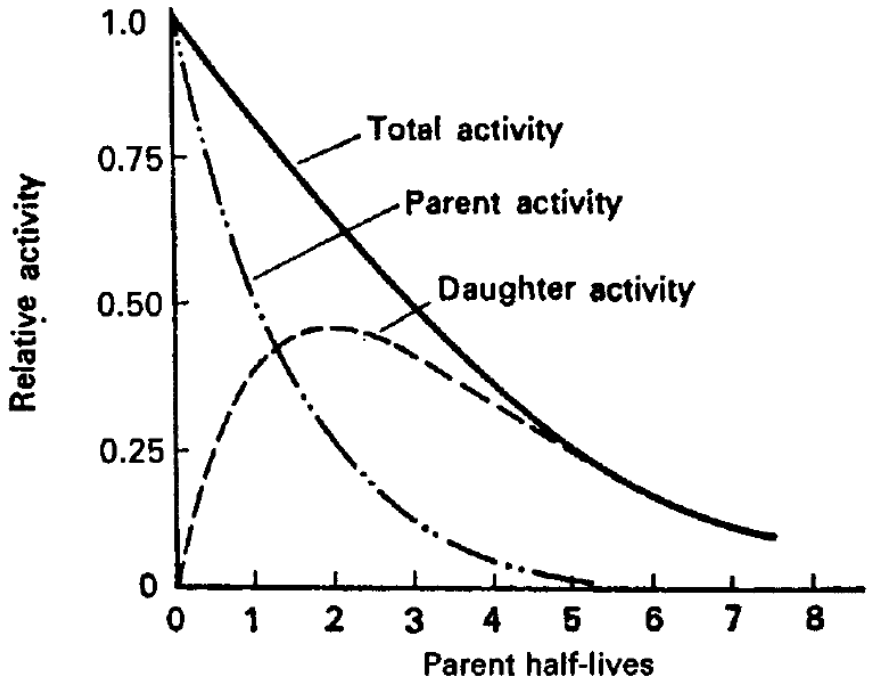

Figure 2.15: No equilibrium between ^{146}Ce (parent) and ^{146}Pr (daughter) [88]

2.4 The basic principles of Monte Carlo simulation

The Monte Carlo simulation method is a simple computer technique that involves conducting a large number of fictitious experiments with random numbers. Its application is ubiquitous and requires no special probability expertise. The only information required is the output-input relationship and the input-output probability distributions. This simulation method is very similar to random experiments, in which the specific outcome is unknown in advance. In this context, Monte Carlo simulation can be a methodical approach to what-if analysis [93,94]. Therefore, the Monte Carlo simulation identifies a statistical distribution for each input parameters. Then we take random samples from each distribution to represent the input variables' values.

We get output parameters for each set of input parameters. Each output parameter represents one of the simulation's outcomes. We collect these results from several simulation runs. Finally, we use statistical analysis to decide what to do next. The output parameter sampling statistics can be used to quantify output variation. The Monte Carlo simulation has many applications in different fields such as simulation and optimization problems, particle physics, nuclear and high energy physics, quantum field theory, environmental sciences, financial market simulations, astrophysics, Semiconductor devices, Light transport calculations, artificial intelligence for games, etc. [93,94]. More information about the Monte Carlo simulation method can be found in the literature [93–97].

Chapter 3. Experimental Setup

3.1 Liquid scintillator container

We used the UG-AB liquid scintillation cocktail in a liquid scintillation counting system. UG-AB is a non-hazardous liquid scintillation cocktail based on the solvent 2,6-Diisopropylnaphthalene (DIPN) [76]. The DIPN-based organic liquid scintillation cocktails have a rise time of about 1 ns and a decay time of about 2.5 to 7 ns [98,99]. We fed the radon source for 48 hours from the air in 700 mL of UG-AB in a sample container made of 1 liter (l) stainless steel (SUS) with Teflon coating inside and 2 mm SUS exterior with a 5-mm-thick glass window. The container was kept open after filling the sample in a dust-free environment at the underground lab for 48 hours and occasionally mixed to allow the radon source to enter the container safely. Radon surrounds us everywhere, but the radon's level varies from one area to another according to different conditions [100–103]. Figure 3.1 shows a liquid scintillator container that is already closed and ready for an experiment.

Figure 3.1: The photograph of the liquid scintillator container.

3.2 Experimental arrangement

A Hamamatsu PMT (H7195), high voltage power supply (HV), and NGT400 were used in this experiment. Figure 3.2 shows a schematic arrangement of the experimental setup. This arrangement involves LSC, HV, PMT, NGT400, and a PC. The LSC, PMT, and NGT400 are photographed and presented in Figure 3.3. The photograph of the detector arrangement with 5- cm-thick lead (Pb) shielding is shown in Figure 3.4.

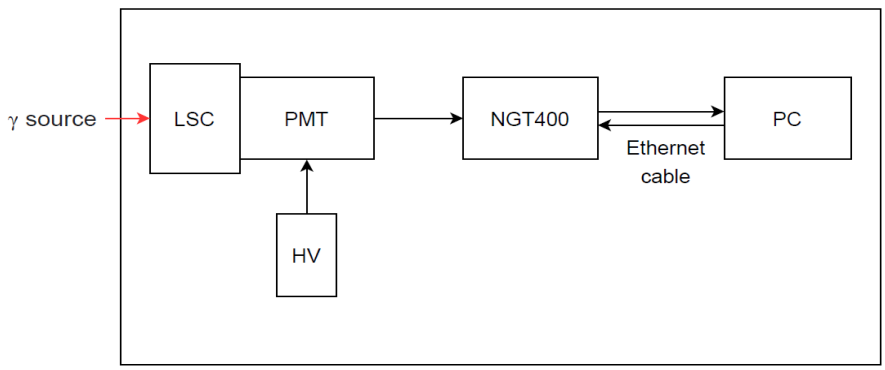

Figure 3.2: The schematic arrangement of the experimental setup.

Figure 3.3: The photograph of LSC, PMT, and NGT400.

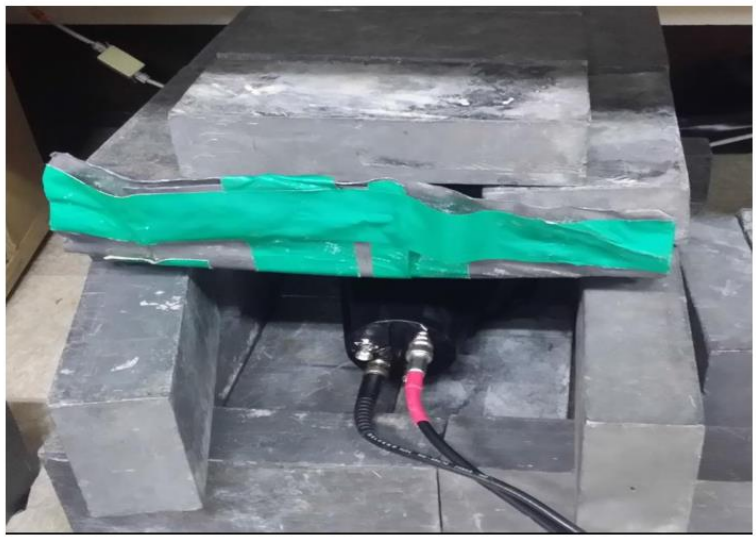

Figure 3.4: A photograph of the detector arrangement with a 5 cm thick Pb shielding.

3.3 Data acquisition

The NGT400 was developed for fast neutron tagging using LSC [104]. The NGT400 can accept an input pulse width between 20 and 1270 ns. The ability of the processing signals is possible up to a 1 MHz input rate by adopting a 400 MS/s flash analog to digital converter (FADC) and a high-speed digital signal processor. It tags signals from a liquid scintillation detector using PSD implemented by the DCC method. The PSD parameters were obtained using equation 3.1.

$$\mathrm{PSD} = \frac{\mathrm{tail}}{\mathrm{body}}\ , \qquad 3.1$$

where the tail denotes the delay charge, and the body denotes the total charge. The total charge was integrated over a 100 ns pulse window range, while the delay charge was integrated from the delay point to the end of the pulse width.

The delay point was set to 20 ns after the pulse's maximum position as shown in figure 2.9 in section 2.2.3. PSD was used to identify α and β in the spectrum. NGT400 performs PSD with 2.5 ns precision. The recorded data by NGT400 is analyzed offline using the C^{++} program and ROOT package [67]. More information about NGT400 can be found in NOTICE Korea [105]. Figure 3.5 shows DCT, the tag time between prompt and delayed events. This is the time difference between two signals. Table 3.1 presents the summary of the target isotopes. The fast sub-chain members from ^{238}U, ^{232}Th, and ^{235}U families can be selected via the time-amplitude analysis [106]. The isotopes with short half-lives are selected based on their characteristic energy and decay-time distributions. The sub-chain ^{214}Bi (Q_β = 3.27 MeV, $T_{1/2}$ = 20 min) → ^{214}Po (Q_α= 7.83 MeV, $T_{1/2}$ = 164 μs) is used for ^{238}U decay series. The sub-chain ^{212}Bi (Q_β = 3.25 MeV, $T_{1/2}$ = 60.55 min) → ^{212}Po (Q_α= 8.95 MeV, $T_{1/2}$ = 0.299 μs) is employed for ^{232}Th decay chains. On the other end the sub-chain ^{219}Rn (Q_α= 6.95 MeV, $T_{1/2}$ = 3.97 s) → ^{215}Po (Q_α= 7.53 MeV, $T_{1/2}$ = 1.78 ms) from ^{235}U decay series is used. The cutting conditions also are required to be set for the specific ROI.

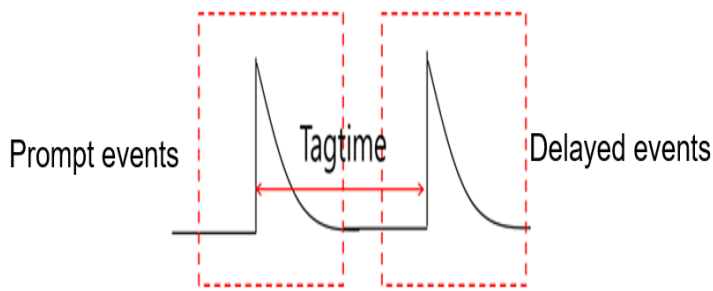

Figure 3.5: The delayed coincidence technique (DCT).

Table 3.1: The summary of the target isotopes.

	^{238}U family	**^{232}Th family**	**^{235}U family**
Mother isotope	^{214}Bi	^{212}Bi	^{219}Rn
	Q_β = 3.27 MeV	Q_β = 2.25 MeV	Q_α = 6.95 MeV
	$T_{1/2}$ = 20 min	$T_{1/2}$ = 60.55 min	$T_{1/2}$ = 3.97 s
Daughter	^{214}Po	^{212}Po	^{215}Po
	Q_α = 7.83 MeV	Q_α = 8.95 MeV	Q_α = 7.53 MeV
	$T_{1/2}$ = 164 μs	$T_{1/2}$ = 300 ns	$T_{1/2}$ = 1.78 ms
Granddaughter	^{210}Pb (unstable)	^{208}Pb (stable)	^{211}Pb (unstable)

Chapter 4. Data analysis

4.1 Calibration of the detector

The calibration of the detector is essential because if it is wrong, it will affect all data analysis of the experiment [107]. The experimental gamma data for calibration were taken in order to have the detector calibrated before using it. Energy calibration, fitting, simulation, and energy resolution at full width at half maximum (FWHM) were performed using the Monte Carlo simulation data. The procedures followed the method presented in a previous study [108]. In our study, the energy calibration fitting procedure that minimizes the difference between the Gaussian broadening of the simulation spectrum and experimental data was performed. The calibration can briefly be summarized as follow: a simulated spectrum is generated corresponding to each gamma source measurement (Fig. 5.4 shows an example of ^{137}Cs spectrums). Energy calibration scaling factor (a) and detector resolution (FWHM) were scanned by customized appropriate step for a minimum testing chi-square value in a specified channel region of interest ($C \pm \Delta C$) around the Compton edge. Corresponding energy for the specified channel C is $E=aC$; (C, E) is used later for the energy calibration curve, and (E, FWHM) is for resolution curve fitting. Uncertainties of FWHM, a, C, and E are determined accordingly. In the simulation, we didn't put the energy resolution of the detector. The detector resolution was obtained by a fitting procedure that minimizes chi-square between Gaussian broadening of simulation spectrum and experimental data. For example, the detector's resolution of a ^{137}Cs peak of 662 keV is around 22%. Due to the finite detector resolution, the 662 keV peak is broadened and cannot be observed in the measurements data. The same

applied to ^{60}Co and ^{22}Na

The gamma calibration function of the UG-AB liquid detector can be expressed using equation 4.1.

$$Y = aX + b, \quad 4.1$$

where Y is the calibrated light output in keV, X is the channel number that corresponds to the deposited energy, and a and b are constants to be calculated. For an example, in the case of radon-filled data from air sources, the equation obtained using this general fitting model, along with the corresponding constants, is presented in equation 4.2:

$$Y = 0.95Channel + 23.02 \quad 4.2$$

As a result, using equation 4.2, all of the data obtained during this measurement were converted to equivalent energy (keV). However, alpha particles have a poor scintillation response in LSC compared to beta particles, resulting in a pulse-height response of approximately 10% of its original nuclear decay energy [81,109–112]. For instance, an alpha particle with 5 MeV energy will appear in a UG-AB LSC with an energy of approximately 0.5 MeV.

The FWHM as a function of electron energy (E) was calculated using equation 4.3.

$$\frac{FWHM}{E} = \sqrt{\alpha^2 + \frac{\beta^2}{E} + \frac{\gamma^2}{E^2}}\ , \quad 4.3$$

where α represents a constant term resulting from the locus-dependent light transmission from the scintillator to the photocathode (geometry effect) . This parameter limits the detector's resolution at high energy [51,54,108,113–115]. A stochastic term β resulting from the statistical behavior of light production and attenuation in the liquid, as well as photon-electron conversion and electron amplification in the PMT. The term γ is the noise term from the PMT and eventually from the electronic amplifier[51,54,108,113–115]. All of these characteristics depend on the detector's construction, and as a result, we anticipate the resolution function to behave differently. In this study, the resolution function was calculated using two parameters of α and γ only. The goodness of fitting is given by R-squared (R^2). The R^2 is given by the variance explained by the model divided by the total variance.

4.2 Fitting function for the Gaussian and exponential decay distribution

The fitting for a Gaussian distribution in ROOT was done using equation 4.4.

$$y = Ae^{-\frac{1}{2}\left(\frac{x-\mu}{\sigma}\right)^2}, \qquad 4.4$$

where y is the Gaussian fitting function, A is the constant depending on fitting, x is the variable on the x-axis, μ is the mean, and σ is the standard deviation. The fitting for exponential decay distribution was done using equation 4.5.

$$y = e^{(p_o + p_1 x)}, \qquad 4.5$$

where y is the exponential fitting function, p_o is the constant depending on fitting, p_1 is the slope (decay constant), and x is the variable on the x-axis. The fitting results are also given with χ^2/ndf parameters, where χ^2 is chi-square and ndf is the number of degrees of freedom. A chi-squared is a weighted sum of squared deviations with the following inputs: variance, observations, and calculated data. The number of degrees of freedom is calculated by subtracting the number of observations from the number of fitted parameters.

4.3 Selection efficiency (SE)

To estimate the efficiency, the detector's cutting conditions based on selection efficiency (SE) were used. The SE is the conditional probability that any single event will pass on the given cutting condition on the detector's region of interest (ROI) [116]. After that, this probability of surviving events is multiplied by 100 % to get the SE. Therefore, these involve PSD, cutting energy for alpha and beta, the fitting formula for alpha and beta, decay time of half-life, etc. This phenomenon is more commonly employed in high-energy physics experiments [67,106,116]. The SE is given by equation 4.6.

$$SE = \frac{\text{selected area (SA) ROI}}{\text{Total area (TA)}} \times 100\ \%, \qquad 4.6$$

where TA is the total probability of geometrical fitting equal to 1, the SA depends on cutting and fitting conditions but is always less than 1. The selection efficiency for half-life, PSD, and alpha events was determined using the geometry's fitting equation, with an error (δ) of approximately $\leq 1.0\%$. The SE of beta events was subjected to the cutting conditions only. The beta

decay spectrum was not fitted because a suitable model was unavailable. The δ in SE was estimated to be $\leq 5.0\%$ due to energy differences at the minimum and maximum levels of beta events from different Bi isotopes. The total efficiency of the detector for each family member of our target isotopes using the method is reported in other literature [67,106].

4.4 Figure of merit (FOM)

A figure of merit (FOM) is a metric that describes the performance of the detector or system. In the presence of gamma rays, any detector with a FOM greater than 1.27 can be deemed to have acceptable PSD for fast neutron detection [117]. FOM can be calculated using the formula presented in equation 4.7 [82].

$$\mathrm{FOM} = \frac{|P_\alpha - P_\beta|}{FWHM_\alpha + FWHM_\beta}\ , \qquad 4.7$$

where P_α and P_β represent the center peak position of α and β obtained in PSD, respectively. $FWHM_\alpha$ and $FWHM_\beta$ are energy resolution of α and β, respectively; calculated from the PSD distributions. While the FOM of the whole system of the targeted isotopes of the system can be determined by using equation 4.8 [43,119,120].

$$\mathrm{FOM} = \frac{\varepsilon^2}{c_b}\ , \qquad 4.8$$

where ε is the efficiency of the system in % and c_b is the background count rate in count per minute (CPM).

4.5 Half-life

The half-life ($T_{1/2}$) was obtained from equation 4.9.

$$T_{1/2} = \frac{0.693}{\lambda} \quad , \tag{4.9}$$

where λ is the decay constant obtained from an exponential fitting function of the half-life decay function. The derivation of this formula can be found in many pieces of literature.

4.6 Activity and minimum detection activity

The count rate is defined by dividing the total counts by the time used for that particular counting. For background (B) counting rate (C_b) and that of sample (S) count rate (C_s) are expressed by $C_b = \frac{B}{T_b}$ and $C_s = \frac{S}{T_s}$, respectively. T_b and T_s are background and sample counting time in minutes, respectively. The net count rate (N) is given by taking the difference between the sample count rate and the background count rate expressed in equation 4.10.

$$N = C_s - C_b \tag{4.10}$$

The associated net standard deviation (σ_N) for the net count rate is given by equation 4.11.

$$\sigma_N = \sqrt{\frac{C_b}{T_b} + \frac{C_s}{T_s}} \tag{4.11}$$

The total count rate in CPM is then given by equation 4.12.

$$N = (C_s - C_b) \pm \sqrt{\frac{C_b}{T_b} + \frac{C_s}{T_s}} \quad 4.12$$

More derivation of counting rate and associated standard deviation can be found in Knoll's book [46]. To convert the count rate in a minute (CPM) to activity (A), we need to consider other factors such as counting efficiency (ε) and sample volume (V_s) in L. T to coverts minutes to seconds, factor a 60 is used. Finally, we get activity in Bq/L. Therefore, activity is given by equation 4.13 [46,121–124].

$$\text{Activity} = \frac{(C_s - C_b) \pm \sqrt{\frac{C_b}{T_b} + \frac{C_s}{T_s}}}{\varepsilon \times V_s \times 60} \text{ (Bq/L)} \quad 4.13$$

The minimum detectable activity (MDA) given by Currie with 95% confidence-interval is presented in equation 4.14 [46,65,120,125–129].

$$\text{MDA} = \frac{2.71 + 4.65\sqrt{C_b T_b}}{\varepsilon \times V_s \times T_s \times 60} \quad 4.14$$

All symbols carry their usual meaning as defined early. The derivation of MDA can be found in the literature [46,125].

Chapter 5. Results and Discussions

5.1. Energy calibrations, resolution, and simulation

The experimental energy and their energy fitting, calibrations, resolution, and simulation were made using three 1 μCi gamma sources, ^{22}Na, ^{60}Co, and ^{137}Cs. The data used for energy calibrations, energy resolution, and simulation were only obtained from their Compton energies. Table 5.1 presents the half-life, different gamma energy, and corresponding Compton energies calculated using equation 2.5 in section 2.1.2. However, the Compton energies for ^{60}Co γ-rays are very close, as shown in table 5.1, which is evident as a combined contribution in figure 5.1. Therefore, the calculations for ^{60}Co were based on the total contributions of their Compton energies.

Table 5.1: Data of the 1 μCi gamma sources used for calibration.

Gamma source	Half-life (years)	Gamma Energy (MeV)	Compton energy (MeV)
^{22}Na	2.6	0.511	0.341
^{137}Cs	30.2	0.662	0.477
^{60}Co	5.3	1.173	0.963
^{22}Na	2.6	1.275	1.062
^{60}Co	5.3	1.332	1.118

5.1.1 Experimental data of ^{22}Na, ^{60}Co, and ^{137}Cs gamma sources and their fitting

Figure 5.1 shows the experimental gamma spectra and their Compton fitting curves. The γ-rays spectra fittings well matched the experimental data.

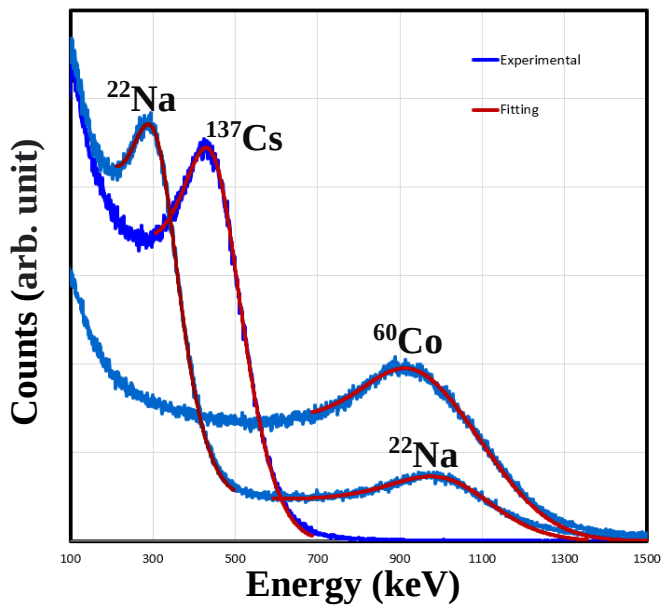

Figure 5.1: The experimental data representation of the Compton edges from ^{22}Na, ^{60}Co, and ^{137}Cs gamma sources and their fitting.

5.1.2 Energy calibration

The energy calibration is the relationship between the γ-rays energy and channel. The energy calibration in Figure 5.2 indicates that the experimental data were well fitted linearly.

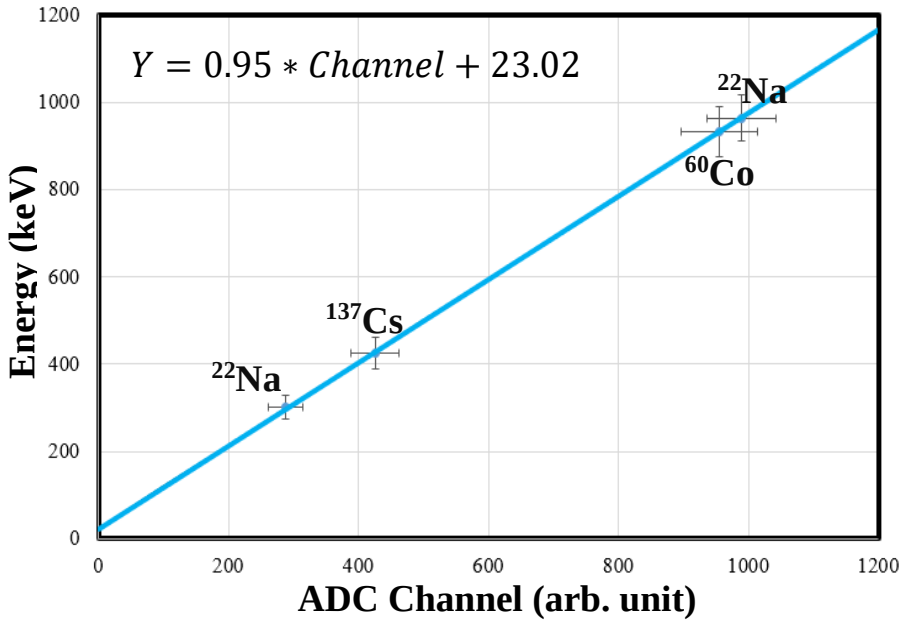

Figure 5.2: The energy calibration using the Compton edges of ^{22}Na, ^{60}Co, and ^{137}Cs.

5.1.3 Energy resolution

Figure 5.3 presents the energy resolutions in terms of FWHM of the UG-AB detector, ranging from 20 to 30% gamma sources used in this experiment. The FWHM obtained in this experiment matched well with the previous study [51].

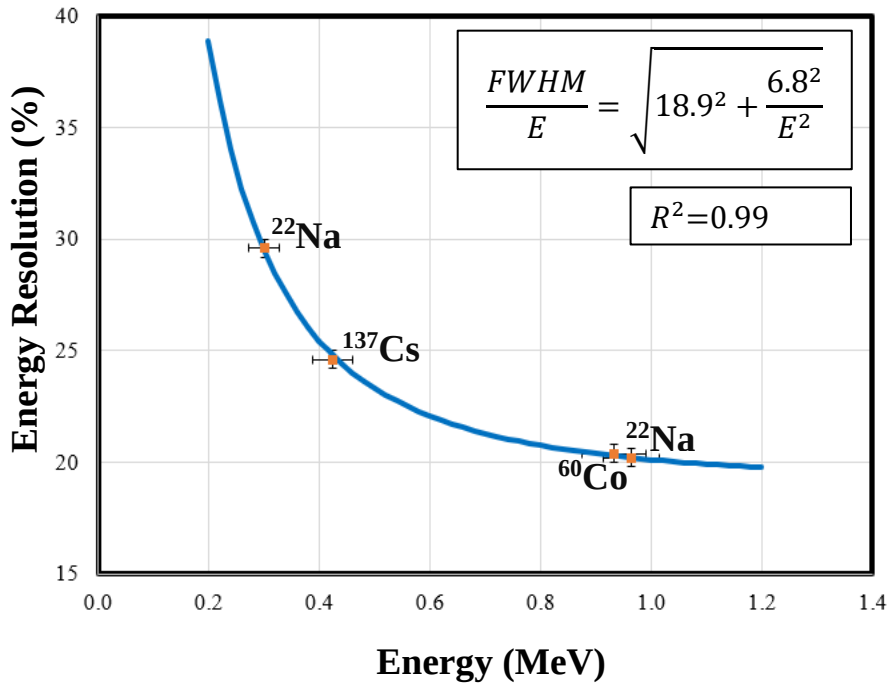

Figure 5.3: The energy resolution (FWHM) result using the Compton edges of ^{22}Na, ^{60}Co, and ^{137}Cs.

5.1.4 Monte-Carlo simulation Energy

Figures 5.4, 5.5, and 5.6 compare the simulated Compton electron spectrum from ^{137}Cs, ^{60}Co, and ^{22}Na gamma sources. The simulations quite match well with the experimental and fitting data.

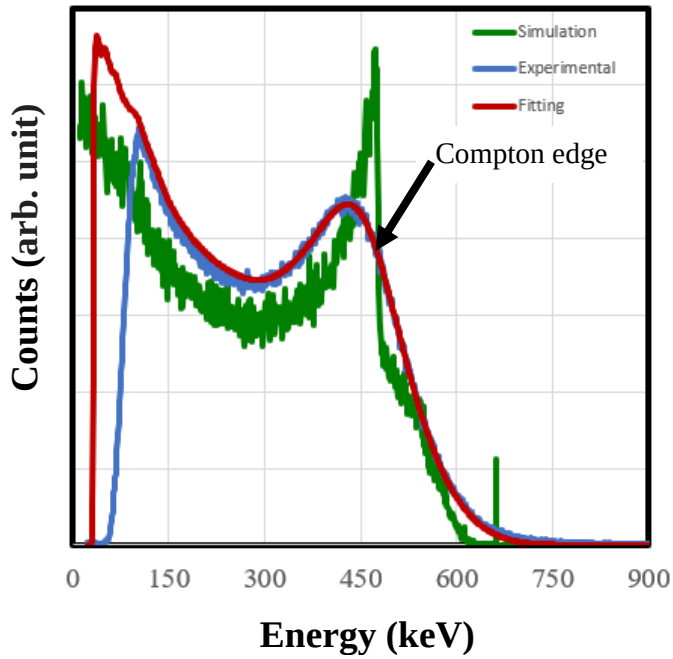

Figure 5.4: Monte-Carlo-simulated Energy spectrum from the ^{137}Cs gamma source.

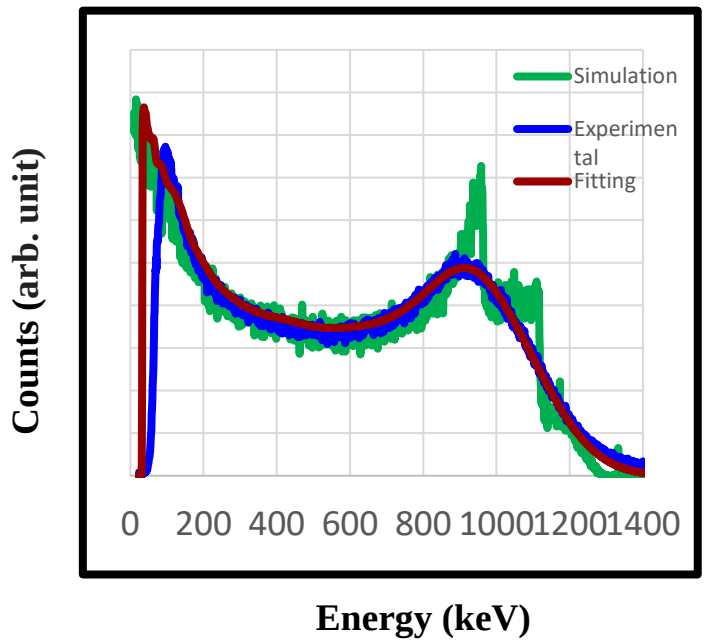

Figure 5.5: Monte-Carlo-simulated Energy spectrum from the ^{60}Co gamma source.

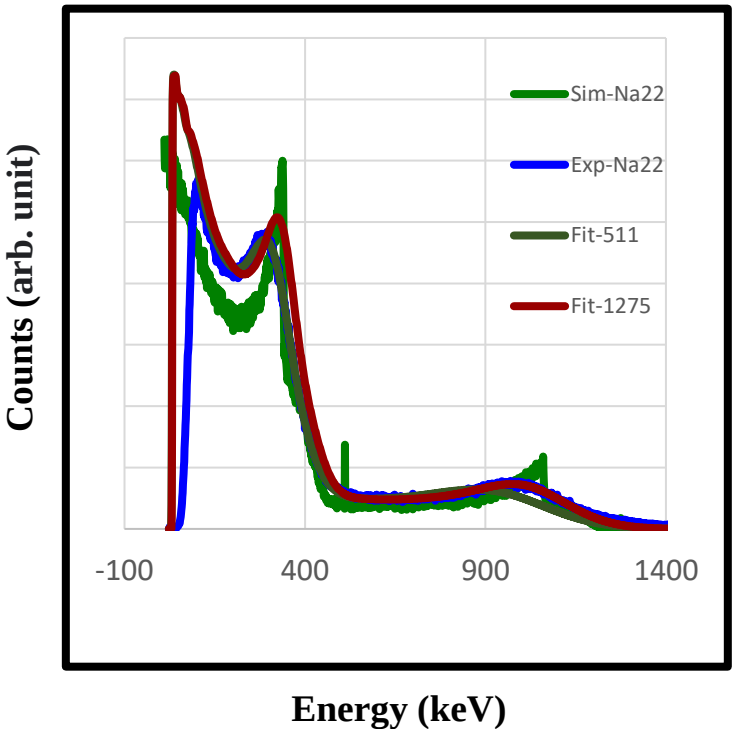

Figure 5.6: Monte-Carlo-simulated Energy spectra from the ^{22}Na gamma source.

5.2. Light quenching

Figure 5.7 shows the light quenching recorded in this technique using the 1 μCi ^{137}Cs gamma source. The calculated light quench based on the channel ratio method was 6.8%.

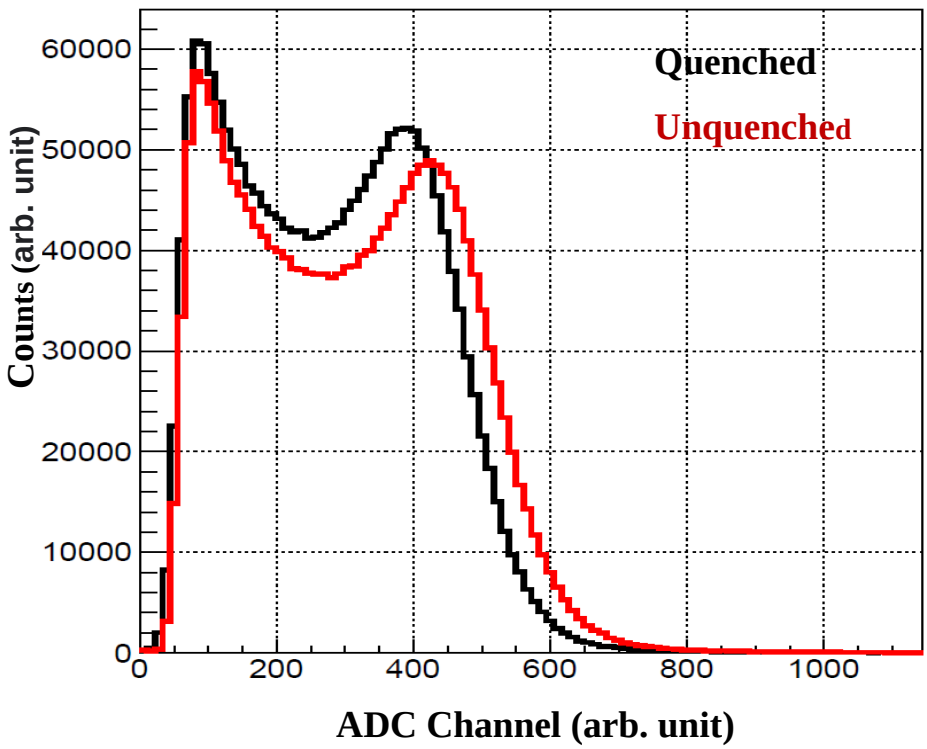

Figure 5.7: The light quenching from 1 μCi ^{137}Cs gamma source.

5.3. Background Measurements

The background measurement was performed for 2328 min of data acquisition for 2 million events. Figure 5.8 shows the background spectrum with pure UG-AB without filling radon from the air. The background count rate for the full spectrum was 859.1 cpm. Because the full spectrum may not be used for calculations, the (ROI) is usually specified in order to limit the background count rate in the specific region [130]. Therefore, the background count rate was found to be 0.32, 0.0095, and 0.021 cpm for ^{222}Rn (^{238}U), ^{220}Rn (^{232}Th), and ^{219}Rn (^{235}U) decay series, respectively. Figure 5.9 indicates the

alpha energy from ^{214}Po (^{238}U family) with the background spectrum in the ROI. The net activity of the sample data can be done by removing the background count rate within the ROI.

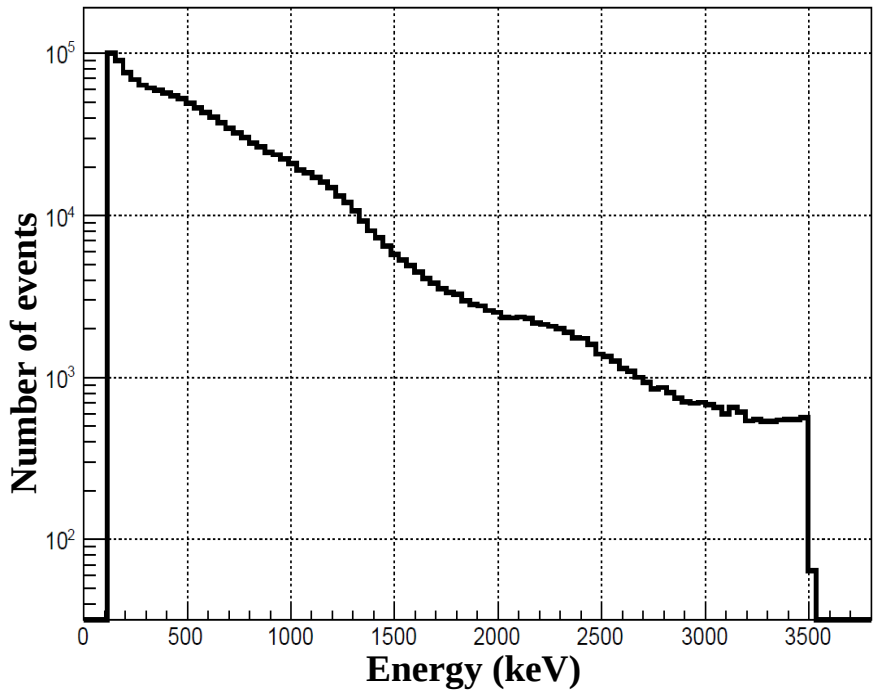

Figure 5.8: The energy spectrum of background measurements below 3.5 MeV data recording (note: y-axis is in the log scale).

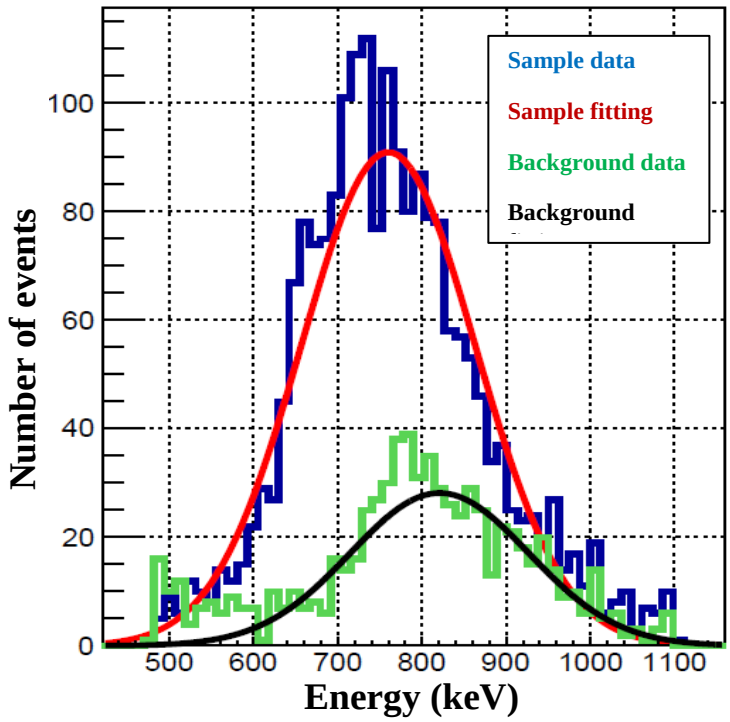

Figure 5.9: The alpha energy from ^{214}Po (^{238}U family) with the background within the same ROI.

5.4. Half-life events from ^{238}U, ^{232}Th, and ^{235}U decay chains

The following three subsections are about the half-life events obtained from ^{238}U, ^{232}Th, and ^{235}U decay chains.

5.4.1 Half-life of ^{214}Po from ^{222}Rn (^{238}U) decay series

To find the half-life from the ^{222}Rn (^{238}U) family, the following cutting conditions were established. The time interval was set between 2 and 820 μs. The short half-life isotope in this decay series is ^{214}Po, with a half-life

of 164.3 μs. The lower limit of 2 μs was set in the time coincidence in order to reject the short ^{212}Bi–^{212}Po coincidence from the ^{232}Th chain. This 2 μs is about seven half-lives of ^{212}Po. ^{212}Po is not expected to be in this cutting condition in such a case. The upper limit of 820 μs was set, about five half-lives of ^{214}Po. It is also required to set the cutting condition of the alpha energy from ^{214}Po. We set the energy range between 480 and 1100 keV and PSD between 0.14 and 0.3. For half-life determination, an exponential function was employed to fit the function in the time distribution. Figure 5.10 indicates the half-life events selected within the ROI for ^{214}Bi $\rightarrow$ ^{214}Po $\rightarrow$ ^{210}Pb (^{238}U family). We found the half-life of ^{214}Po to be 165.4 ± 4.9 μs, which matches well with the expected half-life. The cutting conditions give the SE of $96.7 \pm 1.0\%$ for this decay component.

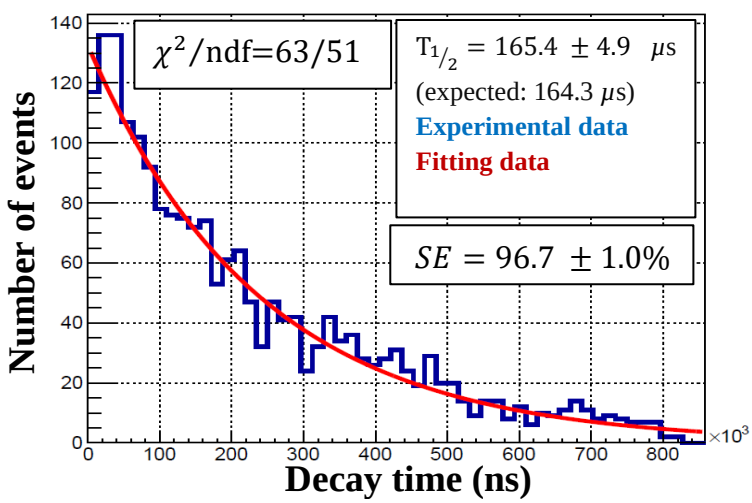

Figure 5.10: The half-life events selected within the ROI for ^{214}Bi$\rightarrow$^{214}Po$\rightarrow$^{210}Pb (^{238}U family) decay with cutting conditions of time between 2 – 820 μs and PSD between 0.14 to 0.3.

5.4.2 Half-life of ^{212}Po from ^{220}Rn (^{232}Th) decay series

We set the following cutting conditions to select ^{212}Po from the ^{220}Rn (^{232}Th) decay series. The time interval of 400-1500 ns. The upper limit is about five half-lives of ^{212}Po. The 300–1600 keV energy range was set, and PSD was between 0.16 and 0.26. Moreover, an exponential function of decay half-life was employed to fit the function. Figure 5.11 displays the selected half-life events within ROI for ^{212}Bi → ^{212}Po → ^{208}Pb (^{232}Th) decay chain. The half-life of ^{212}Po was calculated to be 309.2 ± 47.0 ns which reasonably matched the expected half-life of 300 ns. The cutting condition gives an SE of 37.3 ± 1.0 % for this half-life decay distribution.

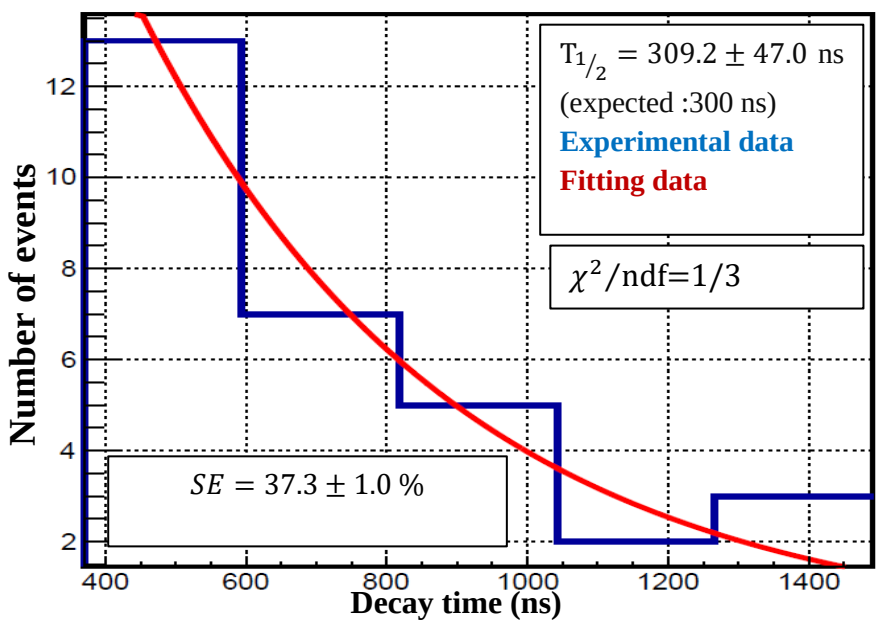

Figure 5.11: The half-life events selected within the ROI for ^{212}Bi → ^{212}Po → ^{208}Pb (^{232}Th family) decay with cutting conditions of time between 400 and 1600 ns and PSD between 0.16 and 0.26

5.4.3 Half-life of ^{215}Po from ^{219}Rn (^{235}U) decay series

To find half-live of ^{215}Po, we set the time difference between 500 and 3600 μs. The upper limit of 3600 μs is near the two half-lives of ^{215}Po. We also set the energy range between 500 and 800 keV and PSD between 0.15 and 0.23. Furthermore, an exponential function of decay half-life was used to fit the time distribution function. Figure 5.12 shows the half-life events within the ROI for ^{219}Rn $\rightarrow$ ^{215}Po $\rightarrow$ ^{209}Pb (^{235}U) decay series. We calculated the half-life of ^{215}Po to be 1.82 ± 0.56 ms. The expected half-life is 1.78 ms. These cutting conditions yielded an SE of $57.3 \pm 1.0\%$ for the half-life decay function.

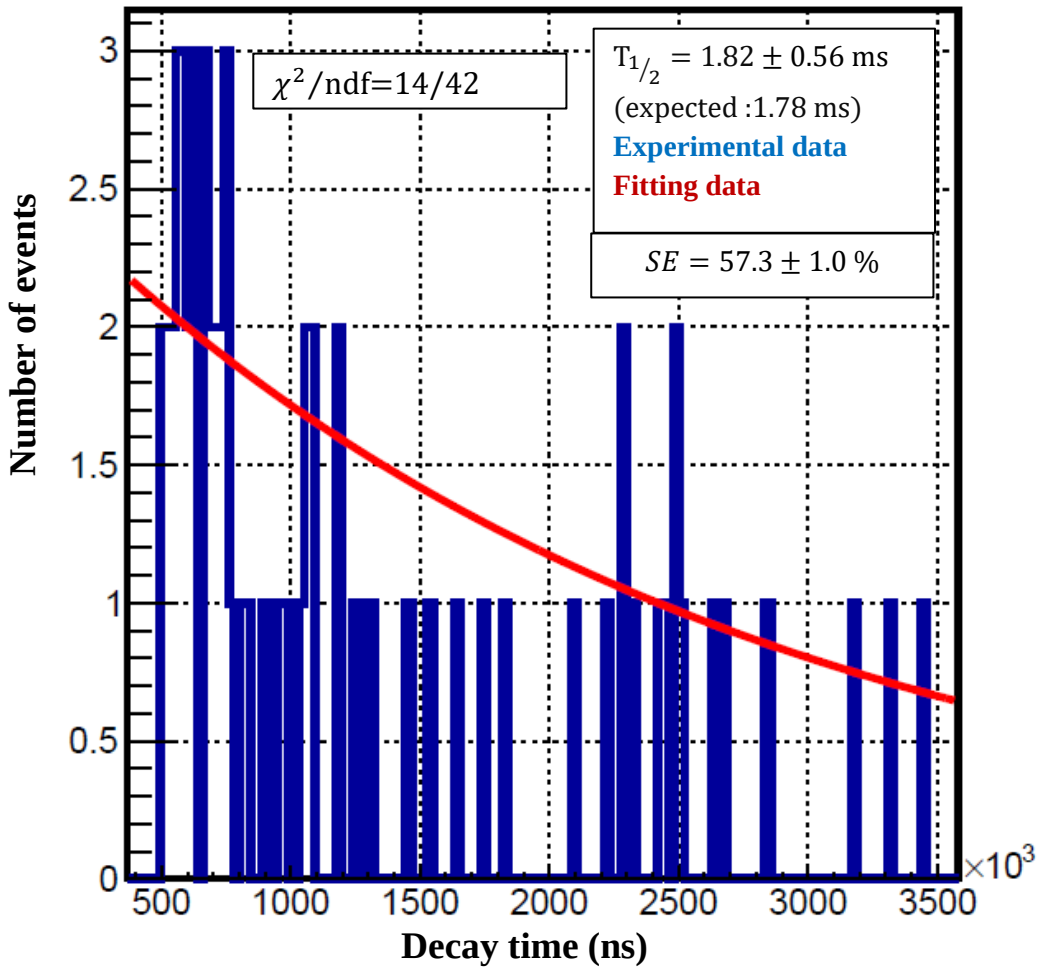

Figure 5.12: The half-life events selected within the ROI for ^{219}Rn →^{215}Po → ^{211}Pb (^{235}U Family) decay with cutting conditions of time between 500 and 3600 μs and PSD between 0.15 and 0.23

5.5 PSD events from ^{238}U, ^{232}Th, and ^{235}U decay chains

This section presents PSD obtained from ^{238}U, ^{232}Th, and ^{235}U decay chains.

5.5.1 PSD events from ^{238}U decay chain

Figure 5.13 indicates the PSD by DCC method for prompt β-decay from ^{214}Bi and delayed events of α-decay from ^{214}Po in the ^{238}U decay chain. The prompt event ^{214}Bi and delayed event ^{214}Po are separated well. Furthermore, the calculated FOM and SE are 0.90 and 97.2±1.0% in these cutting conditions.

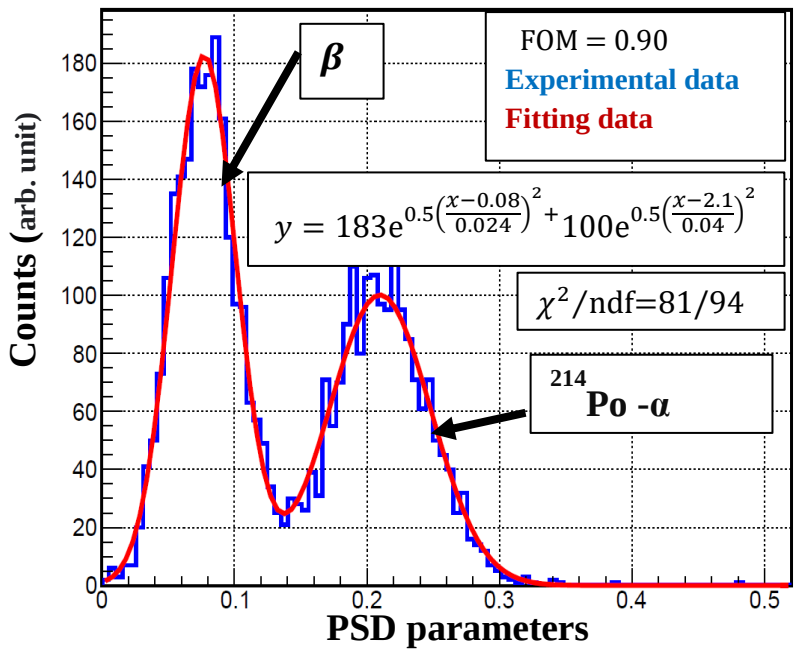

Figure 5.13: PSD for prompt ^{214}Bi and delayed events ^{214}Po from the ^{238}U decay chain.

5.5.2 PSD events from ^{232}Th decay chain

Figure 5.14 displays the PSD using the DCC method for prompt β-decay of ^{212}Bi and delayed ^{212}Po α-decay events from the ^{232}Th decay chain. The prompt event of ^{212}Bi and delayed of ^{212}Po alpha particle events were well

separated with a FOM of 0.95. These cutting conditions gave an SE of 88.1±1.0% for PSD from ^{232}Th decay chains.

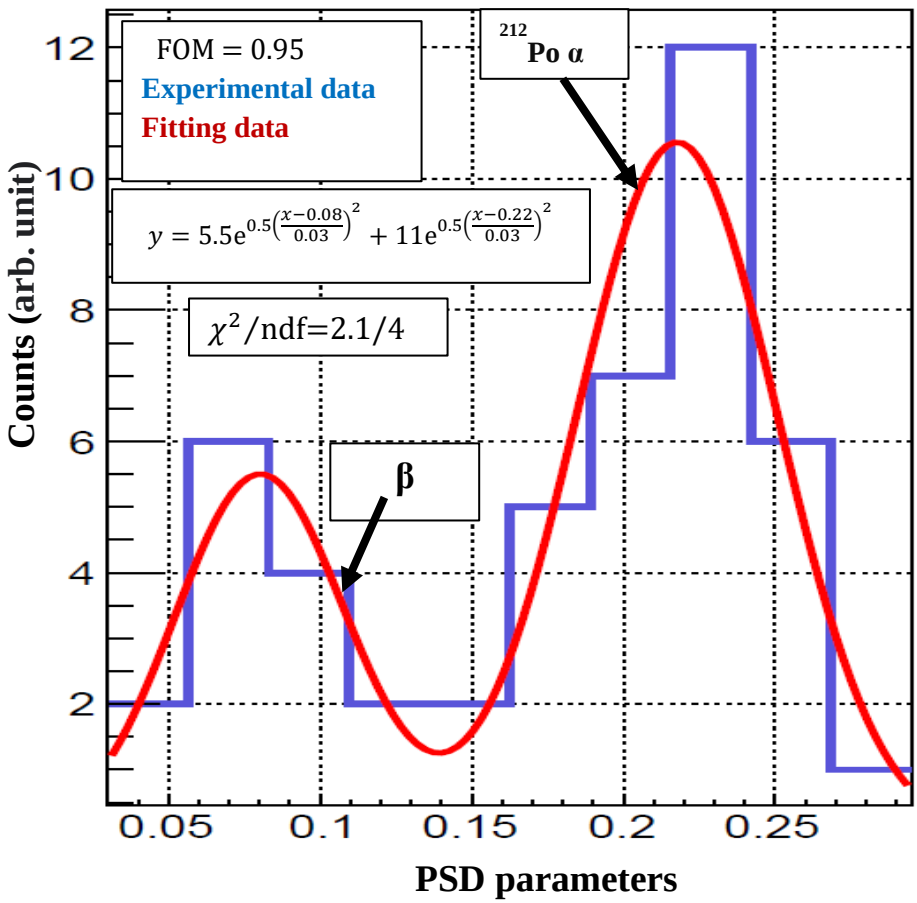

Figure 5.14: PSD for prompt ^{212}Bi and delayed events ^{212}Po from the ^{232}Th decay chain.

5.5.3 PSD events from ^{235}U decay chain

Figure 5.15 indicates the PSD using the DCC method for prompt α-decay of ^{219}R and delayed events α-decay ^{215}Po from the ^{235}U decay series. The prompt ^{219}R and delayed events ^{215}Po are marginal separated. However,

after applying cutting conditions for each event, we obtained results that were not bad. The PSD was able to identify these events. The results will be presented in the following sections. These cutting conditions give the SE of PSD 63.3%.

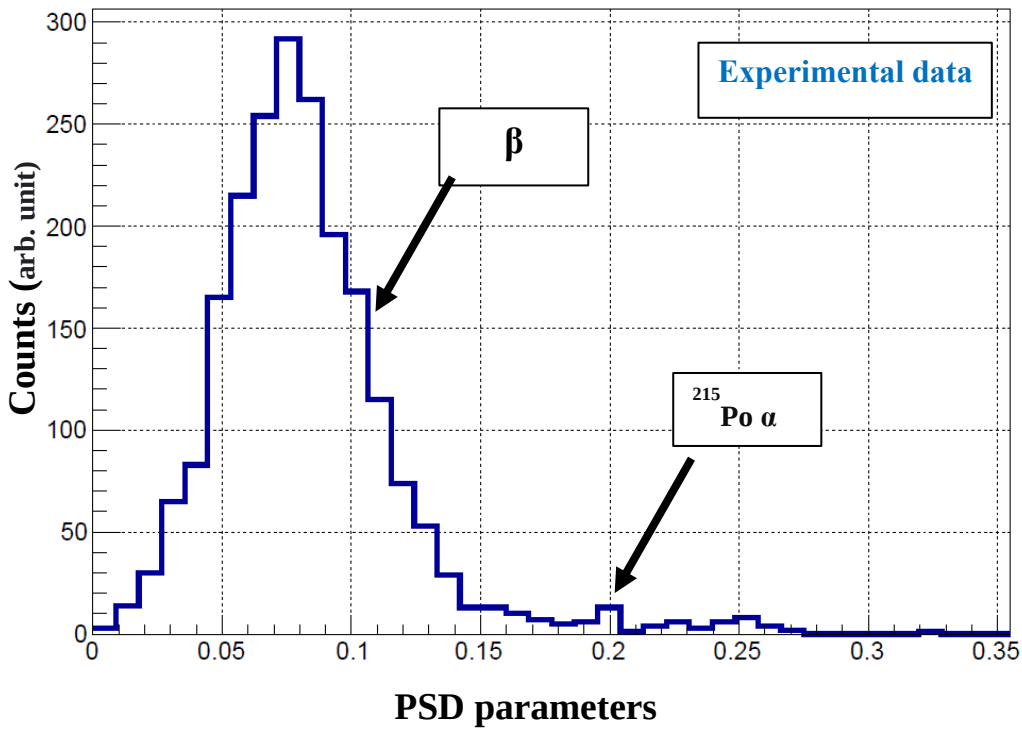

Figure 5.15: PSD for the prompt ^{219}Rn and delayed events ^{215}Po from the ^{235}U decay chain.

5.6. Delay alpha events from ^{238}U, ^{232}Th, and ^{235}U decay chains

In this section, the delayed alpha events from ^{222}Rn (^{238}U), ^{220}Rn (^{232}Th), and ^{219}Rn (^{235}U) decay chains will be presented and discussed.

5.6.1 Delayed alpha-particle events from ^{214}Po (^{238}U) decay chain

The cutting conditions for PSD, decay time, and energy distributions were the same as those in the previous section of 5.4. We select ^{214}Po from the ^{238}U decay chain using PSD by the DCC method, as explained, in section 5.5. To identify the α-particle event from ^{214}Po, we set the energy range as 480 – 1100 keV, the PSD parameter between 0.14 and 0.3, and the cutting time as 2 – 820 μs. These cutting conditions on the ROI give SE of $99.6 \pm 1.0\%$ for α-particle from ^{214}Po with equivalent energy (E_{eq}) of 759.8 ± 103 keV. The mean energy is within the acceptable energy of the expected Q_α = 7.83 MeV. Figure 5.16 identifies alpha energy from the ^{214}Po (^{238}U) decay chain.

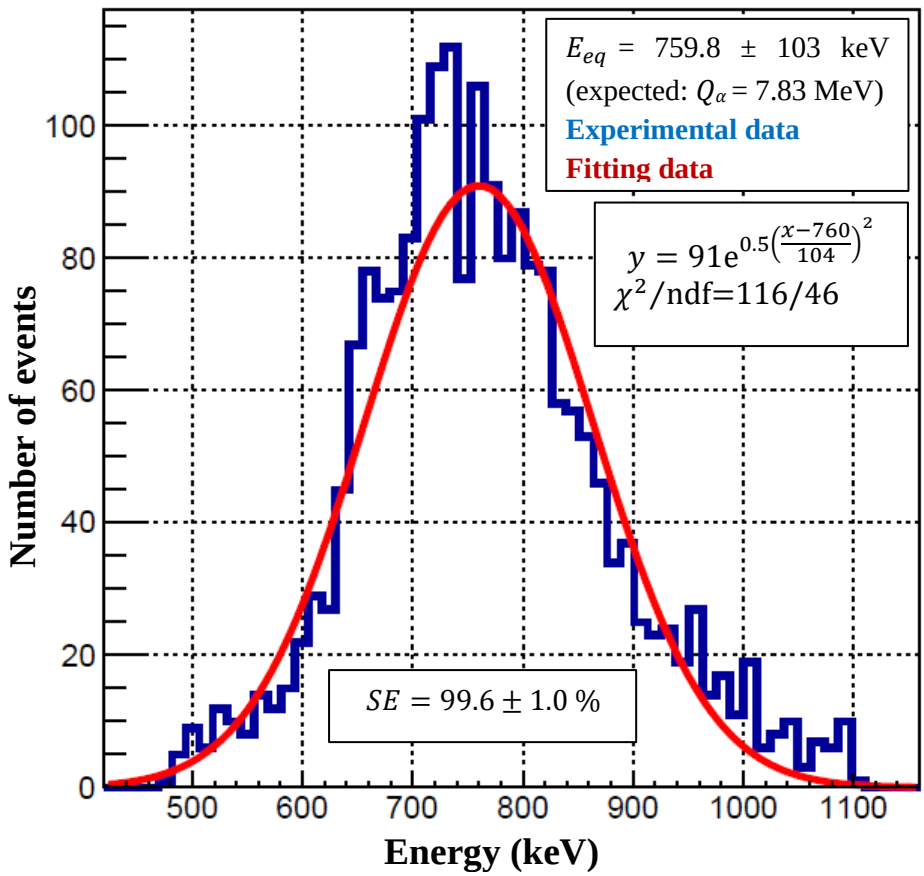

Figure 5.16: The alpha energy from the ^{214}Po (^{238}U) decay chain with cutting conditions of energy between 480 and 1100 keV, time between 2 and 820 μs, and PSD between 0.14 and 0.3.

5.6.2 Delayed alpha-particle events from ^{212}Po (^{232}Th) decay chain

We selected the alpha event of the ^{212}Po (^{232}Th) decay chain using the PSD parameters between 0.16 and 0.26. we also set cutting time between 400 to 1500 ns and the energy range between 300 and 1600 keV. Figure 5.17

identifies alpha energy from the ^{212}Po (^{232}Th) decay chain. The conditions we set on the ROI gave an SE of $96.7 \pm 1.0\%$ for the α-particle ^{212}Po with an E_{eq} of 859 ± 195 keV while the expected one is Q_α = 8.95 MeV. The energy falls within the expected one.

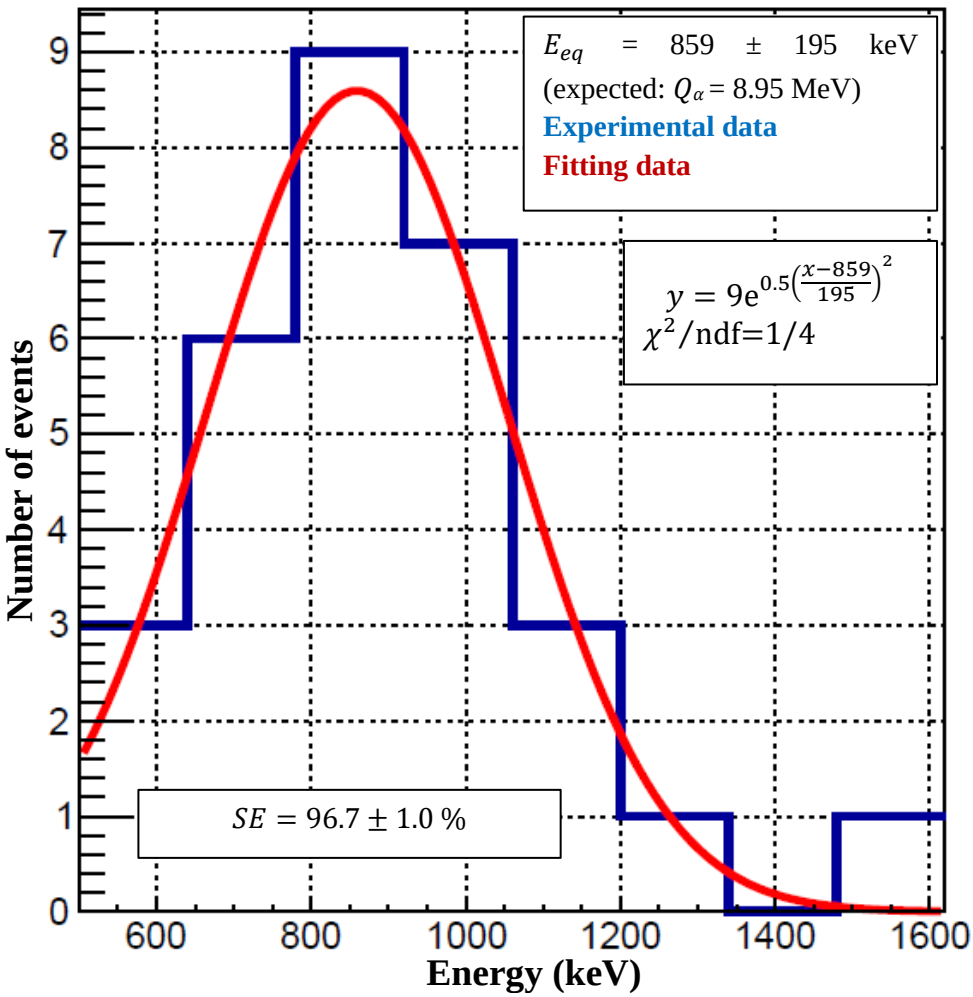

Figure 4.17: The alpha energy from the ^{212}Po (^{232}Th) decay chain with cutting conditions of energy between 300 and 1600 keV, time between 400 and 1600 μs, and PSD between 0.16 and 0.26.

5.6.3 Delayed alpha-particle events from ^{215}Po (^{235}U) decay chain

The α-particle events from the ^{215}Po were obtained using PSD by the DCC method. We set the cutting energy as 500 – 800 keV, cutting time between 500 and 3500 μs, and PSD between 0.16 and 0.26. Figure 5.18 shows the alpha energy from the ^{215}Po (^{235}U) decay chain. The cutting conditions on the ROI gave us an SE of $93.8 \pm 1.0\%$ for the α-particle ^{215}Po with E_{eq} of 712.6 ± 56.82 keV. The energy falls within the range of the expected Q_α = 7.53 MeV).

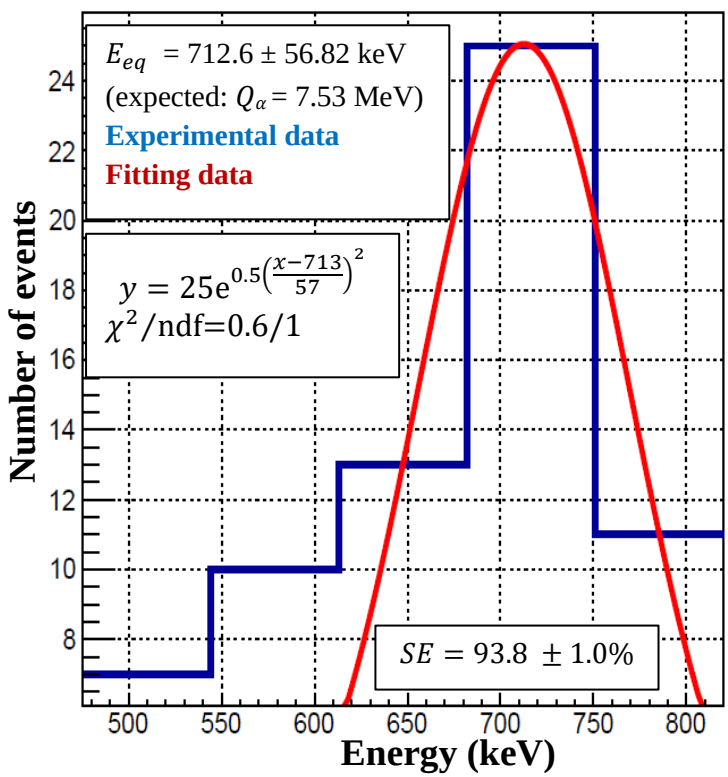

Figure 5.18: The alpha energy from the ^{215}Po (^{235}U) decay chain with cutting conditions of energy between 500 and 800 keV, time between 500 and 3500 μs, and PSD between 0.15 and 0.23.

5.7. Prompt beta events from ^{238}U and ^{232}Th and alpha events from ^{235}U decay chains

In this subsection, we will present and discuss the results obtained from the prompt beta events from ^{238}U and ^{232}Th and alpha from ^{235}U decay chains.

5.7.1 Prompt beta-particle events **from ^{214}Bi** (^{238}U) decay chain

The β-particle event for prompt ^{214}Bi was selected by employing the PSD method. We set the cutting condition for the energy between 100 and 3000 keV, time between 2 and 820 μs, and the PSD between 0.14 and 0.3. Figure 5.19 shows beta-particle events from ^{214}Bi (^{238}U) decay chain. The maximum energy ($Q_{\beta max}$) distribution of ^{214}B is 3.27 MeV. These cutting conditions gave the SE of 90.0 ± 5.0 % for the β-particle ^{214}Bi energy distribution.

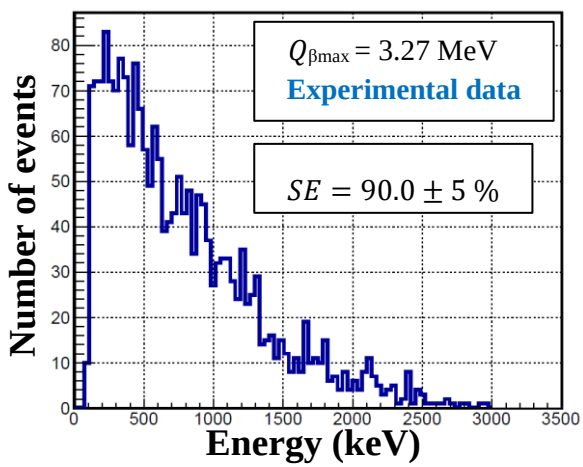

Figure 5.19: The beta-particle events from the ^{214}Bi (^{238}U) decay chain with cutting conditions of energy between 100 to 3000 keV, time between 2 and 820 μs, and PSD between 0.14 and 0.3.

5.7.2 Prompt beta-particle events **from ^{212}Bi** (^{232}Th) decay chain

The prompt β-particle event from the ^{212}Bi through the cutting conditions of energy between 150 and 2500 keV and cutting time as 400 – 1600 μs and PSD between 0.16 and 0.26. Figure 5.20 shows the beta-particle events from ^{212}Bi (^{232}Th) decay chain. The $Q_{\beta max}$ distribution of ^{212}B is 3.25 MeV. These cutting conditions yielded SE of 66.26 % for the ^{212}Bi (^{232}Th) decay chain

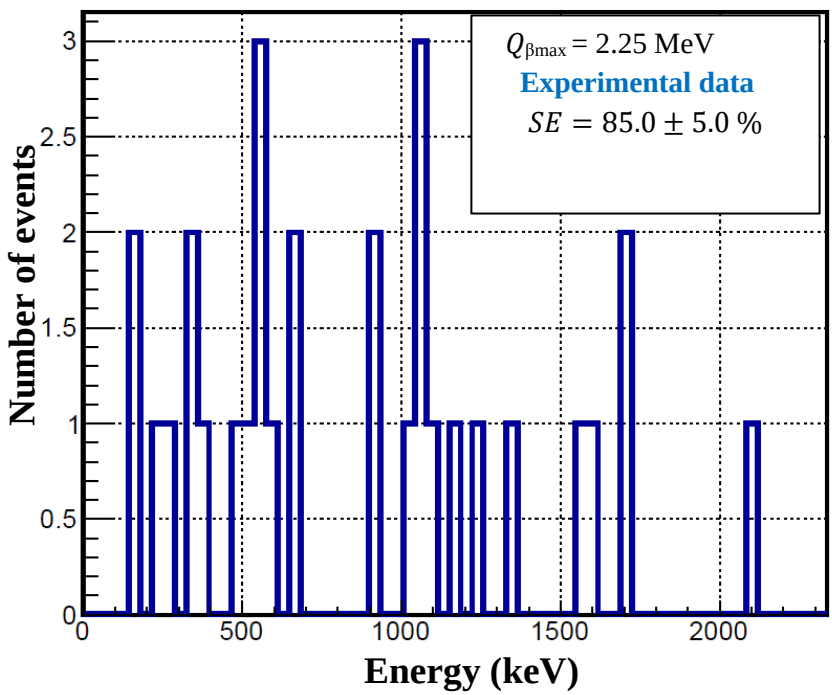

Figure 5.20: The beta-particle events from ^{212}Bi (^{232}Th) decay chain with cutting conditions of energy between 150 and 2500 keV, time between 400 and 1600 μs, and PSD between 0.16 and 0.26

5.7.3 Prompt α-particle events **from ^{219}Rn** (^{235}U) decay chain

The prompt α-particle event from the ^{219}Rn was identified by setting the cutting condition on PSD between 0.15 and 0.23 to differentiate it from another α-particle from ^{215}Po. We set the cutting energy between 500 and 1000 keV and cutting time between 500 and 3600 μs. These cutting conditions gave SE of 96.9$\pm$1.0% for the α-particle from ^{219}Rn with the E_{eq} of 712.6 ± 56.82 keV. The calculated energy falls within the expected one Q_{α} = 7.53 MeV. Figure 5.21 shows alpha-particle events from the ^{219}Rn (^{235}U) decay chain.

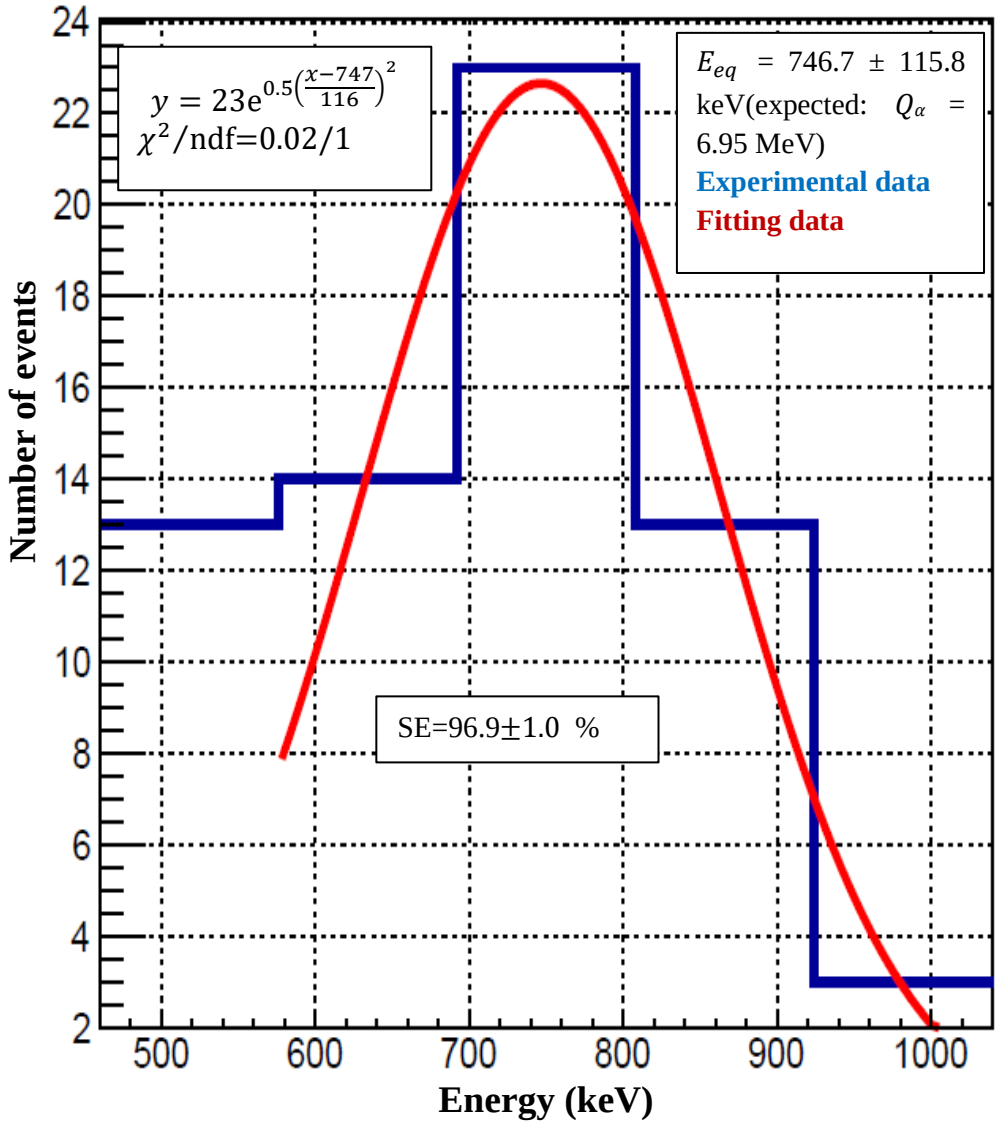

Figure 4.21: The alpha-particle events from the ^{219}Rn (^{235}U) decay chain with cutting conditions of energy between 500 and 1000 keV, time between 500 and 3600 μs, and PSD between 0.15 and 0.23.

5.8. The detector's efficiency and sensitivity

Tables 5.2, 5.3, and 5.4 present the summary of the cutting conditions and SE for the ^{238}U, ^{232}Th, and ^{235}U families, respectively. From these tables, we found the counting efficiency of alpha particles to be 99.6% for ^{214}Po, 96.7% for ^{212}Po, 96.5% for ^{219}Rn, and 93.8% for ^{215}Po. This is consistent with other previously studies [41,56,111,131]. The total efficiency of the detector system was determined to be 84.3 $\pm$ 5.3 % for ^{222}Rn (^{238}U family), 27.0 $\pm$ 5.3% for ^{220}Rn (^{232}Th family), and 33.0 $\pm$ 3.0% for ^{219}Rn (^{235}U family).

Detector sensitivity is the most important parameter to consider regarding detection techniques. It represents the lowest level at which the detection technique can distinguish between a sample signal and the background signal. The MDA of a technique is the lowest amount of activity that can be practically detected with a 95% confidence level. If the level of activity in a sample is lower than the MDA, the measuring device will not be able to detect it during that particular measurement. The Currie formula can be used to compute the detector sensitivity in MDA in Bq/L using equation 4.16, presented in section 4.6. The MDA calculated with a sample volume of 700 mL were 1.7, 1.0, and 1.2 mBq/L for ^{222}Rn (^{238}U decay series), ^{220}Rn (^{232}Th decay series), and ^{219}Rn (^{235}U decay series), respectively. The background and sample counting times were 38.8 and 35.3 h, respectively. The MDA obtained using this technique is better than many studies using LSC. For example, the MDA of 1.7 mBq/L obtained from ^{222}Rn (^{238}U decay series) is much better compared to the previous technique based on LSC for the determination of ^{222}Rn from the ^{238}U decay series [132–141]. Table 5.5 summarizes the parameters used to calculate MDA from ^{238}U, ^{232}Th, and ^{235}U families.

Table 5.2: Summary of the cutting conditions and selection efficiency (SE) from the ^{238}U decay chain.

(^{238}U Family)	Cutting conditions	SE (%)	δ (%)
Half-life of ^{214}Bi→^{214}Po→^{210}Pb	2 < dt < 820 μs	96.7	1.0
PSD parameters selection	0.14 < PSD < 0.3	97.2	1.0
α Energy product from ^{214}Po	480 < E_{α} < 1100 keV	99.6	1.0
β Energy product from ^{214}Bi	100 < E_{β} < 3000 keV	90.0	5.0
Total efficiency (ε)		**84.3**	**5.3**

Table 5.3: Summary of the cutting conditions and selection efficiency (SE) from the ^{232}Th decay chain.

(^{232}Th Family)	Cutting conditions	SE (%)	δ (%)
Half-life of $^{212}Bi \rightarrow ^{212}Po \rightarrow ^{208}Pb$	$0.4 < dt < 1.5\ \mu s$	37.3	1.0
PSD parameters selection	$0.16 < PSD < 0.26$	88.1	1.0
α Energy product from ^{212}Po	$300 < E_{\alpha} < 1600$ keV	96.7	1.0
β Energy product from ^{212}Bi	$150 < E_{\beta} < 2500$ keV	85.0	5.0
Total efficiency (ε)		**27.0**	**5.3**

Table 5.4: Summary of the cutting conditions and selection efficiency (SE) from the ^{235}U decay chain.

(^{235}U Family)	Cutting conditions	SE (%)	δ (%)
Half-life of ^{219}Rn→^{215}Po→^{211}Pb	500 < dt < 3600 μs	57.3	1.0
PSD parameters selection	0.15 < PSD < 0.23	63.3	1.0
α Energy product from ^{215}Po	500 < E_α < 800 keV	93.8	1.0
α Energy product from ^{219}Rn	500 < E_α < 1000 keV	96.9	1.0
Total efficiency (ε)		**33.0**	**3.0**

Table 5.5: Summary of the parameters used to calculate minimum detectable activity (MDA) from ^{238}U, ^{232}Th, and ^{235}U families.

(^{238}U Family)	Values and units	δ(%)
ε	84.3%	5.3
C_b	0.32 CPM	1.2
T_b	2328.0 min	1.2
Ts	2120.6 min	1.7
MDA	**1.7 mBq/L**	**5.8**
(^{232}Th Family)	**Values and units**	**δ(%)**
ε	27.0%	5.3
C_b	0.0095 CPM	0.2
T_b	2328.0 min	0.2
Ts	2120.6 min	0.2
MDA	**1.0 mBq/L**	**5.3**
(^{235}U Family)	**Values and units**	**δ(%)**
ε	33.0%	3.0
C_b	0.021 CPM	0.3
T_b	2328.0 min	0.3
Ts	2120.6 min	0.2
MDA	**1.2 mBq/L**	**3.0**

5.9. Activity concentrations from ^{222}Rn (^{238}U), ^{220}Rn (^{232}Th), and ^{219}Rn (^{235}U) families

The activity concentrations (specific activity) of the sample in Bq/L were calculated using equation 4.15 presented in section 4.6. The specific activity of pure UG-AB after radon filling was determined to be 18.1 mBq/L from the ^{222}Rn (^{238}U) decay series, approximately ten times higher than MDA. ^{220}Rn from ^{232}Th decay series and ^{219}Rn from ^{235}U decay series had less specific activity than their MDA. According to a previous study, radiation measurements should not be recorded as less than MDA since they may underestimate the radioactivity level [142]. As a result, the specific activity for the ^{220}Rn (^{232}Th) decay series and ^{219}Rn (^{235}U) decay series is reported as 0.44 and 0.73 mBq/L, respectively.

Chapter 6. Summary and Conclusion

By infusing radon gas from the atmosphere into a 700 mL UG-AB using a 1 L SUS container, a novel LSC technique was used to measure the three naturally occurring radon isotopes simultaneously. The measured half-lives of ^{214}Po, ^{212}Po, and ^{215}Po were 165.3 μs, 309.2 ns, and 1.82 ms, respectively. It matches their expected half-lives of 164.3μs, 300 ns, and 1.78 ms. In our technique, the counting efficiency of alpha particles was near 100%. Furthermore, the total efficiency of the counting system was found to be 84.3% for the ^{222}Rn (^{238}U) decay series, 27.0% for the ^{220}Rn (^{232}Th) decay series, and 33.0% for the ^{219}Rn (^{235}U) decay series. The MDA values for ^{222}Rn (^{238}U), ^{220}Rn (^{232}Th), and ^{219}Rn (^{235}U) decay series were determined to be 1.7, 1.0, and 1.2 mBq/L. Considering the MDA obtained in this study, the detection sensitivity can be improved more in a deep underground laboratory with enhanced shielding. To our best knowledge, this is the first report on successfully measuring all three naturally occurring radon isotopes simultaneously using the LSC system. The radon activity levels of ^{222}Rn (^{238}U), ^{220}Rn (^{232}Th), and ^{219}Rn (^{235}U) decay chains in water samples can be determined well using this novel technique.

References

[1] CNSC, Natural Background Radiation, Can. Nucl. Saf. Comm. (2020). https://nuclearsafety.gc.ca/eng/pdfs/Fact_Sheets/Fact-Sheet-Background-Radiation-eng.pdf.

[2] Division of Environmental Health Office of Radiation Protection, Background Radiation Natural versus Man-Made, Washington State Department of Health (2002). https://doh.wa.gov/sites/default/files/legacy/Documents/Pubs//320-063_bkvsman_fs.pdf.

[3] M.I. Ojovan, W.E. Lee, An Introduction to Nuclear Waste Immobilisation, (2005). https://doi.org/https://doi.org/10.1016/B978-0-08-044462-8.X5000-5.

[4] M. Baskaran, Handbook of environmental isotope geochemistry, Handb. Environ. Isot. Geochemistry. 1–2 (2012) 1–951. https://doi.org/10.1007/978-3-642-10637-8.

[5] L. Kölbel, T. Kölbel, U. Maier, M. Sauter, T. Schäfer, B. Wiegand, Water–rock interactions in the Bruchsal geothermal system by U–Th series radionuclides, Geotherm. Energy. 8 (2020). https://doi.org/10.1186/s40517-020-00179-4.

[6] C.L.Tan, Big Gaps and Short Bridges: A Model for Solving the Discontinuity Problem, Answers Res. J. 9 (2016) 149–162. https://answersresearchjournal.org/model-solving-discontinuity-problem.

[7] M.M. Kescher, Deep-water circulation and detrital provenance in the South Pacific, from the present day until 240,000 years ago. Evidence from Nd, Sr and Pb isotopes and Rare Earth Elements, Ph.D. Thesis.

(2014). https://doi.org/10.13140/2.1.4675.8089.

[8] W.G. Mook, Environmental isotopes in the hydrological cycle: Principles and applications, Volume I: Introduction: Theory, Methods, Review, Int. Hydrol. Program. IHP-V. 1 (2001) 1–165. http://www-naweb.iaea.org/napc/ih/documents/global_cycle/Environmental Isotopes in the Hydrological Cycle Vol 1.pdf.

[9] F.D. Sowby, Annals of the ICRP, Ann. ICRP. 6 (1981) 1. https://doi.org/10.1016/0146-6453(81)90127-5.

[10] US EPA, What Are the Sources of Ionizing Radiation?, State Univ. New Jersey - RUTGERS. (1996) 1–3. http://www.nj.gov/dep/rpp/llrw/download/fact03.pdf.

[11] P.M. Lantz, D. Mendez, M.A. Philbert, Radon, smoking, and lung cancer: The need to refocus radon control policy, Am. J. Public Health. 103 (2013) 443–447. https://doi.org/10.2105/AJPH.2012.300926.

[12] Y.W. Jin, S. Seo, Radon and Lung Cancer: Disease Burden and High-risk Populations in Korea, J. Korean Med. Sci. 33 (2018) e210. https://doi.org/10.3346/jkms.2018.33.e210.

[13] A. Noverques, G. Verdú, B. Juste, M. Sancho, Experimental radon exhalation measurements: Comparison of different techniques, Radiat. Phys. Chem. 155 (2019) 319–322. https://doi.org/https://doi.org/10.1016/j.radphyschem.2018.08.002.

[14] WHO, Indoor Radon a Public Health Perspective, (2014). https://apps.who.int/iris/bitstream/handle/10665/44149/9789241547673_eng.pdf.

[15] J.M. Samet, E. Avila-Tang, P. Boffetta, L.M. Hannan, S. Olivo-Marston, M.J. Thun, C.M. Rudin, Lung cancer in never smokers: Clinical epidemiology and environmental risk factors, Clin. Cancer Res.

15 (2009) 5626–5645. https://doi.org/10.1158/1078-0432.CCR-09-0376.

[16] S.H. Kim, W.J. Hwang, J.S. Cho, D.R. Kang, Attributable risk of lung cancer deaths due to indoor radon exposure, Ann. Occup. Environ. Med. 28 (2016) 8–11. https://doi.org/10.1186/s40557-016-0093-4.

[17] C. Kranrod, Y. Tamakuma, M. Hosoda, S. Tokonami, Importance of discriminative measurement for radon isotopes and its utilization in the environment and lessons learned from using the RADUET monitor, Int. J. Environ. Res. Public Health. 17 (2020) 1–14. https://doi.org/10.3390/ijerph17114141.

[18] IARC, Man-Made Mineral Fibres and Radon IARC Monographs on the Evaluation of the Carcinogenic Risks to Humans Volume 43 IARC, IARC Publ. (1988). https://publications.iarc.fr/Book-And-Report-Series/Iarc-Monographs-On-The-Identification-Of-Carcinogenic-Hazards-To-Humans/Man-Made-Mineral-Fibres-And-Radon-1988.

[19] BEIR, Health Effects of Exposure to Radon, National Academies Press, 1999. https://doi.org/10.17226/5499.

[20] US EPA, EPA facts about radon, (2014). https://semspub.epa.gov/work/HQ/176336.pdf.

[21] J. Eikenberg, R & D projects of the PSI radioanalytical laboratory, Nord. Nucl. Saf. (2013) 18–22. http://www.nks.org/download/RADIOANALYSIS2013/rw14eikenberg.pdf.

[22] IRSN, New dose coefficients for radon , recommended in ICRP Publication 137 Explanatory note, Rep. PSE-DSNTE/2018-00002 (2018). https://www.irsn.fr/EN/publications/technical-publications/Pages/technical-health.aspx.

[23] E. Vañó, C.J. Miller, M.M. Rehani, K. Kang, M. Rosenstein, P. Ortiz-López, S. Mattsson, R. Padovani, A. Rogers, Annals of the ICRP, ICRP Publication 135: Diagnostic Reference Levels in Medical Imaging, Sage (2017). https://doi.org/10.1177%2F0146645317717209.

[24] C. Wanke, B. Szermerski, L. Geworski, Measurement of Rn-219 with Alphaguard radon monitors, Appl. Radiat. Isot. 151 (2019) 310–316. https://doi.org/10.1016/j.apradiso.2019.03.041.

[25] M.M. Cooper, A.W. Elzerman, C.M. Lee, Environmental chemistry, J. Chem. Educ. 78 (2001) 1169. https://doi.org/10.1021/ed078p1169.

[26] International Trade Administration, Tanzania mining- Country Commercial Guide, Int. Trade Adm. (2021) 1–12. https://www.trade.gov/country-commercial-guides/malaysia-agricultural-sector.

[27] Victoria state government (VSG), What Does Minerals Exploration Involve ?, Victoria Gov. State. (2020). https://earthresources.vic.gov.au/__data/assets/pdf_file/0008/459440/What-Does-Minerals-Exploration-Involve-December-2020.pdf.

[28] A.Dixit, “Introducing uranium mining requires long-term planning, which includes surveys of the selected exploration sites, soil assessments, building public awareness and capacity building.” Five years on, Tanzania’s progress in uranium exploration, IAEA. (2018) 6–7. https://www.iaea.org/sites/default/files/publications/magazines/bulletin/bull59-2/5920607.pdf.

[29] K.A. Miller, K.F. Thompson, P. Johnston, D. Santillo, An overview of seabed mining including the current state of development, environmental impacts, and knowledge gaps, Front. Mar. Sci. 4 (2018).

https://doi.org/10.3389/fmars.2017.00418.

[30] Victoria state government (VSG), Understanding minerals exploration - Earth Resources, Victoria Gov. State. (2021) 2–3. https://earthresources.vic.gov.au/community-and-land-use/understanding-exploration.

[31] D.A. Mwalongo, Reporting Uranium Resource And Project Activities in Tanzania FOR 2012-2013, United Nations Econ. Comm. Eur. (2013) 9–12. https://unece.org/fileadmin/DAM/energy/se/pp/unfc_egrm/unfc_ws_IAEA_CYTED_UNECE_Santiago_July2013/12_July/7_Mwalongo_Tanzania_CS.pdf.

[32] E. Kimaro, Uranium Mining In The United Republic Of Tanzania: Current Status, Challenges And Opportunities, IAEA. (2016) 206–209. https://inis.iaea.org/collection/NCLCollectionStore/_Public/49/097/49097441.pdf.

[33] Theburningofrome, Theburningofrome.com, Theburningofrome. (2020) 1–7. https://www.theburningofrome.com/users-questions/where-uranium-is-mined-in-tanzania/.

[34] L. Nkuba, Y. Sungita, Radioactivity Levels in Maize from High Background Radiation Areas and Dose Estimates for the Public in Tanzania, Phys. Sci. Int. J. 13 (2017) 1–8. https://doi.org/10.9734/psij/2017/31697.

[35] G.R. Ltd, Tanzanian uranium exploration continues (2022). https://www.listcorp.com/asx/gla/gladiator-resources/news/tanzania-uranium-exploration-continues-2688591.html.

[36] A. El-Taher, An Overview of Instrumentation for Measuring Radon in Environmental Studies, J. Radiat. Nucl. Appl. 3 (2018) 135–141.

https://doi.org/10.18576/jrna/030302.

[37] J.N. Corrêa, S.A. Paschuk, H.R. Schelin, L. Barbosa, T. Sadula, C.A. Matsuzaki, Measurements of Radon Concentration Levels in Drinking Water at Urban Area of Curitiba (Brazil)., 2009 Int. Nucl. Atl. Conf. (2009). https://inis.iaea.org/collection/NCLCollectionStore/_Public/41/109/41109065.pdf.

[38] V. Jobbágy, T. Altzitzoglou, P. Malo, V. Tanner, M. Hult, A brief overview on radon measurements in drinking water, J. Environ. Radioact. 173 (2017) 18–24. https://doi.org/10.1016/j.jenvrad.2016.09.019.

[39] US EPA, Methods, occurrence and monitoring document for ^{222}Rn from drinking water, (1999). https://nepis.epa.gov/Exe/ZyPDF.cgi/20001XKG.PDF?Dockey=20001XKG.PDF.

[40] X. gui Feng, Q. ge He, J. chen Wang, J. Chen, A method for optimum PSA setting in the absence of a pure α or β emitter and its application in the determination of ^{237}Np/^{233}Pa, Appl. Radiat. Isot. 93 (2014) 114–119. https://doi.org/https://doi.org/10.1016/j.apradiso.2014.01.029.

[41] I. Stojković, B. Tenjović, J. Nikolov, N. Todorović, Possibilities and limitations of color quench correction methods for gross alpha/beta measurements, Appl. Radiat. Isot. 122 (2017) 164–173. https://doi.org/10.1016/j.apradiso.2017.01.041.

[42] X. Hou, X. Dai, Environmental liquid scintillation analysis, Elsevier Inc., 2020. https://doi.org/10.1016/b978-0-12-814395-7.00002-7.

[43] A. Chapon, G. Pigrée, V. Putmans, G. Rogel, Optimization of liquid scintillation measurements applied to smears and aqueous samples

collected in industrial environments, Results Phys. 6 (2016) 50–58. https://doi.org/10.1016/j.rinp.2016.01.018.

[44] D.R. Hill, X-Ray Interaction with Matter, Princ. Diagnostic X-Ray Appar. (1975) 39–47. https://doi.org/10.1007/978-1-349-02452-0_5.

[45] M. Ragheb, Gamma rays interaction with matter, Energy. (2008) 1–25. https://silo.tips/download/gamma-rays-interaction-with-matter.

[46] G.F. Knoll, Radiation Detection and Measurement, 4th Edition, Wiley(2010). ISBN-10:9780470131480, https://www.wiley.com/en-us/Radiation+Detection+and+Measurement%2C+4th+Edition-p-9780470131480.

[47] C. Mahuvava, F.C.P. Du Plessis, Monte Carlo evaluation of the dose perturbation effect of hip prostheses for megavoltage photon radiotherapy, Phys. Medica. 31 (2015) S7. https://doi.org/10.1016/j.ejmp.2015.07.108.

[48] IAEA, Diagnostic Radiology Physics: A Handbook for Teachers and Students, International Atomic Energy Agency publication, 2014. https://www.iaea.org/publications/8841/diagnostic-radiology-physics.

[49] M. Katsura, J. Sato, M. Akahane, A. Kunimatsu, O. Abe, Current and novel techniques for metal artifact reduction at CT: Practical guide for radiologists, Radiographics. 38 (2018) 450–461. https://doi.org/10.1148/rg.2018170102.

[50] J.E. Parks, The Compton Effect-- Compton Scattering and Gamma Ray Spectroscopy Rough Draft 08 / 01 / 2009, Mod. Phys. Lab. (2015). http://www.phys.utk.edu/labs/modphys/Compton Scattering Experiment.pdf.

[51] S.-Y.-L.-T. Zhang, Z.-Q. Chen, R. Han, X.-Q. Liu, R. Wada, W.-P. Lin, Z.-X. Jin, Y.-Y. Xi, J.-L. Liu, F.-D. Shi, Study on gamma response

function of EJ301 organic liquid scintillator with GEANT4 and FLUKA, Chinese Phys. C. 37 (2013) 126003. https://doi.org/10.1088/1674-1137/37/12/126003.

[52] B. Wan, X.Y. Zhang, L. Chen, H.L. Ge, F. Ma, H. Bin Zhang, Y.Q. Ju, Y. Bin Zhang, Y.Y. Li, X.W. Xu, Digital pulse shape discrimination methods for n-γ separation in an EJ-301 liquid scintillation detector, Chinese Phys. C. 39 (2015) 1–6. https://doi.org/10.1088/1674-1137/39/11/116201.

[53] K. Brandenburg, A. Emilja, P. Aaron, Calibration of EJ-301 , a Liquid Scintillator, (2015) 1–10. https://london.physics.ucdavis.edu/~reu/REU14/Papers/brandenburg.pdf.

[54] J. Yan, R. Liu, C. Li, L. Jiang, X.X. Lu, T.H. Zhu, Energy calibration of a BC501A liquid scintillator using a γ-γ coincidence technique, Chinese Phys. C. 34 (2010) 993–997. https://doi.org/10.1088/1674-1137/34/7/012.

[55] J. Qin, C. Lai, B. Ye, R. Liu, X. Zhang, L. Jiang, Characterizations of BC501A and BC537 liquid scintillator detectors, Appl. Radiat. Isot. 104 (2015) 15–24. https://doi.org/10.1016/j.apradiso.2015.06.008.

[56] M.F. L'Annunziata, M.J. Kessler, Liquid Scintillation Analysis, Handb. Radioact. Anal. (2012) 423–573. https://doi.org/10.1016/b978-0-12-384873-4.00007-4.

[57] H. Kang, S. Min, B. Seo, C. Roh, S. Hong, J.H. Cheong, Low energy beta emitter measurement: A review, Chemosensors. 8 (2020) 1–42. https://doi.org/10.3390/chemosensors8040106.

[58] D.M. Taylor, Radiochemistry and nuclear chemistry, 1995. https://doi.org/10.1016/0969-8043(95)90023-3.

[59] S. Min, H. Kang, B. Seo, J. Cheong, C. Roh, S. Hong, A review of nanomaterial based scintillators, Energies. 14 (2021) 1–43. https://doi.org/10.3390/en14227701.

[60] N. Tsoulfanidis, S. Landsberger, Measurement detection of radiation, 4th edition, 2015.

[61] J.A.S. and M.E.P. Simon R. Cherry, Physics in Nuclear Medicine, 2012. https://doi.org/10.2967/jnumed.113.123125.

[62] B.T.Y. Anagida, Incident particle Charged particle X- or γ -ray, 94 (2018) 75–97.

[63] Chanho Kim, Wonhi Lee, Alima Melis, Abdallah Elmughrabi, Kisung Lee, Chansun Park, A Review of Inorganic Scintillation Crystals for Extreme Environments, Crystals. 11 (2021) 669.

[64] A. Courti, P. Bouisset, P. Chevallier, Beta spectrometry for environmental radioactivity measurements, Radioprotection. 37 (2002) C1-911-C1-916. https://doi.org/10.1051/radiopro/2002223.

[65] J.W. Bae, H.R. Kim, Plastic scintillator beta ray scanner for in-situ discrimination of beta ray and gamma ray radioactivity in soil, Nucl. Eng. Technol. 52 (2020) 1259–1265. https://doi.org/10.1016/j.net.2019.11.013.

[66] M.M. Khalil, Basic science of PET imaging, 2016. https://doi.org/10.1007/978-3-319-40070-9.

[67] H.J. Kim, S.-H. Lee, Development of a Large-Volume Fast-Neutron Detector for Environmental Neutron Monitoring, J. Korean Phys. Soc. 53 (2006) 3182–3186. https://doi.org/https://doi.org/10.3938/jkps.53.3182.

[68] A. ParveenI.Siddavatam, Methods of pulse shape discrimination (PSD), Int. Technol. Conf. 66 (2014) 219. https://www.ijaiem.org/ITechCON-

2014/INST-02.pdf.

[69] T.Montaruli, PID : ToF principle Scintillators in brief, Univ. Wisconsin–Madison. (2006). https://user-web.icecube.wisc.edu/~tmontaruli/801/lect11.pdf.

[70] C. Lynde, E. Montbarbon, M. Hamel, A. Grabowski, C. Frangville, G.H.V. Bertrand, G. Galli, F. Carrel, V. Schoepff, Z. El Bitar, Optimization of the Charge Comparison Method for Multiradiation Field Using Various Measurement Systems, IEEE Trans. Nucl. Sci. 67 (2020) 679–687. https://doi.org/10.1109/TNS.2020.2966886.

[71] M.J. Cieślak, K.A.A. Gamage, R. Glover, Pulse shape discrimination characteristics of stilbene crystal, pure and ^{6}Li loaded plastic scintillators for a high resolution coded-aperture neutron imager, J. Instrum. 12 (2017) P07023–P07023. https://doi.org/10.1088/1748-0221/12/07/P07023.

[72] R. Aryaeinejad, J.K. Hartwell, D.F. Spencer, Comparison between digital and analog pulse shape discrimination techniques for neutron and gamma ray separation, IEEE Nucl. Sci. Symp. Conf. Rec. 1 (2005) 500–504. https://doi.org/10.1109/NSSMIC.2005.1596302.

[73] B. Wan, X.Y. Zhang, L. Chen, H.L. Ge, F. Ma, H. Bin Zhang, Y.Q. Ju, Y. Bin Zhang, Y.Y. Li, X.W. Xu, Digital pulse shape discrimination methods for n-γ separation in an EJ-301 liquid scintillation detector, Chinese Phys. C. 39 (2015) 1–5. https://doi.org/10.1088/1674-1137/39/11/116201.

[74] H.J.Kim, M.J. Kim, J.Y. Lee, S.C. Kim, S.Y.Kim, Development of multifunctional digital pulse processing module for particle identification in liquid scintillator, LSC2017. (2017) 1–15. http://lsc2017.nutech.dtu.dk/wp-content/uploads/2-Kim-Multifuction-

digital-puls-ID181.pdf.

[75] U.C. de Venezuela, Radiation Detection and Measurement, 79–114 (2005). http://www.saber.ula.ve/imagenologia/chapter7 radiation detection medicion.pdf.

[76] R. Edler, Cocktails for Liquid Scintillation Counting, PerkinElmer. (2015) 11. https://www.perkinelmer.com/lab-solutions/resources/docs/APP_Cocktails-for-Liquid-Scintillation-Counting-011940_01.pdf.

[77] PerkinElmer, counting application Total solutions for liquid scintillation counting applications — from PerkinElmer, Perkinelmer. (2015). https://resources.perkinelmer.com/lab-solutions/resources/docs/BRO_ScintillationCocktailsAndConsumables.pdf.

[78] The Department of Environmental Health and Safety (EHS), Principles and Applications of Liquid Scintillation Counting, Dep. Environ. Heal. Saf. (2004) 1–15. https://ehs.psu.edu/sites/ehs/files/lsc_theory_of_operation_part_1.pdf.

[79] G.B. Collins, Liquid Scintillation Counting, J. Am. Chem. Soc. 81 (1959) 4122–4123. https://doi.org/10.1021/ja01524a095.

[80] J. Fons Castells, Development of Analytical Methodologies for Rapid Determination of Alpha and Beta Emitters by Liquid Scintillation Spectrometry in Water Samples, Univ. Barcelona. Dep. d'Enginyeria Química i Química Analítica. (2016) 228. http://hdl.handle.net/10803/404352.

[81] S.P.D. Bhade, P.J. Reddy, S. Anilkumar, R. V. Kolekar, R.K. Singhal, R. Singh, Study of liquid scintillation alpha spectral properties, Appl. Radiat. Isot. 122 (2017) 121–126.

https://doi.org/10.1016/j.apradiso.2017.01.017.

[82] J. Thomson, Application Note: Use and preparation of quench curves in LSC, Perkinelmer (2004) 1–6. https://resources.perkinelmer.com/corporate/cmsresources/images/44-167821app_use-and-preparation-of-quench-curves-in-liquid-scintillation-counting.pdf.

[83] E.H. Borai, Y.F. Lasheen, A.F. Seliman, Assessment of Quench Indicating Parameters (QIP) of an Alternative Scintillation Cocktail Mixture by Low Level Liquid Scintillation Counting, World J. Chem. 2 (2007) 1–9. http://www.idosi.org/wjc/2(1)07/1.pdf.

[84] S. Rothchild, Advances in Tracer Methodology, 1966. https://doi.org/10.1021/ac60235a771.

[85] J. Thomson, Quench & Quench Curves, Triskem-International. (2002). https://www.triskem-international.com/scripts/files/59bd7f0fe4c9f6.07016594/james_thomson_quench_and_quench_curves.pdf.

[86] US NRC, Liquid Scintillation Counting 6/21/2011 1, U.S. Nucl. Regul. Comm. (2011). https://www.nrc.gov/docs/ML1122/ML11229A718.pdf.

[87] M.F. L'Annunziata, A. Tarancón, H. Bagán, J.F. García, Liquid scintillation analysis: principles and practice, 2020. https://doi.org/10.1016/b978-0-12-814397-1.00006-6.

[88] P. Alaei, Introduction to Health Physics: Fourth Edition, 2008. https://doi.org/10.1118/1.3021454.

[89] M.A. Thompson, Determination of ^{226}Ra in Fish, McMaster Univ. (2012) 1–96. https://macsphere.mcmaster.ca/bitstream/11375/11836/1/fulltext.pdf.

[90] A. Dash, F.F. Knapp, M.R.A. Pillai, Industrial radionuclide generators: A potential step towards accelerating radiotracer investigations in industry, RSC Adv. 3 (2013) 14890–14909. https://doi.org/10.1039/c3ra41639a.

[91] J.J. d. Vries, N.W. Arnell, NATURAL ISOTOPES OF ELEMENTS OTHER THAN H, C, O, Earth. 21 (2004) 1–24. http://www-naweb.iaea.org/napc/ih/documents/global_cycle/vol I/cht_i_12.pdf.

[92] M.L. Richardson, B. Amini, Teaching Radiology Physics Interactively with Scientific Notebook Software, Acad. Radiol. 25 (2018) 801–810. https://doi.org/10.1016/j.acra.2017.11.024.

[93] S. Raychaudhuri, Introduction to Monte Carlo Simulation, Winter Simul. Conf. Arch. (2008) 91–100. https://informs-sim.org/wsc08papers/012.pdf.

[94] J. Menčík, Introduction to Experimental Analysis, University of Pardubice, 2017. https://dk.upce.cz/bitstream/handle/10195/66961/Introduction to Experimental Analysis.pdf?sequence=1.

[95] R.Y. Rubinstein, D.P. Kroese, Simulation and the Monte Carlo Method, third, Wiley, Hoboken, NJ, USA, 2016. https://doi.org/10.1002/9781118631980.

[96] K. Mitev, C. Dutsov, P. Cassette, B. Sabot, Time-domain based evaluation of detection efficiency in liquid scintillation counting, Sci. Rep. 11 (2021) 1–16. https://doi.org/10.1038/s41598-021-91873-1.

[97] G. a Terejanu, Tutorial on Monte Carlo Techniques, Univ. South Carolina. (2013) 1–15. http://www.cse.sc.edu/~terejanu/files/tutorialMC.pdf.

[98] C. Dutsov, Studies on the Applications of the Triple-to-double

Coincidences Ratio Method for Primary Activity Standardization using Liquid Scintillation Counting, Ph.D. Thesis, Sofia Univ. “St. Kliment Ohridski.” (2021). https://physica.dev/files/phd_thesis.pdf.

[99] P. Lombardi, G. Ranucci, F. Ortica, A. Romani, Decay time and pulse shape discrimination of liquid scintillators based on novel solvents, Nucl. Instruments Methods Phys. Res. Sect. A Accel. Spectrometers, Detect. Assoc. Equip. 701 (2013) 133–144. https://doi.org/10.1016/j.nima.2012.10.061.

[100] C. Bowie, S.H.U. Bowie, Radon and health, Lancet. 337 (1991) 409–413. https://doi.org/10.1016/0140-6736(91)91177-V.

[101] K. Kim, Y. Kim, K. Kim, Efforts to deliver accurate information on radon in Korea, Int. Comm. Radiol. Prot. (2019) 2019. https://www.icrp.org/admin/Kim-Kyo-Youn-Efforts-to-deliver-accurate-information-on-radon-in-Korea.pdf.

[102] J.M. Zielinski, D.B. Chambers, Mapping of residential radon in the world, IAEA (2010). https://inis.iaea.org/search/search.aspx?orig_q=RN:43011999

[103] IAEA, Radiation Protection Against Radon in Workplaces Other Than Mines, IAEA Pub. No.33. 1–79 (2003). https://www-pub.iaea.org/MTCD/Publications/PDF/Pub1168_web.pdf

[104] H.J. Kim, E.J. Kim, S.Y. Kim, Development of a neutron tagger module using a digital pulse shape discrimination method, IEEE Nucl. Sci. Symp. Conf. Rec. (2008) 2917–2919. https://doi.org/10.1109/NSSMIC.2008.4774976.

[105] NOTICE Korea, NGT400(Neutron Tagging Module), accessed March 15, 2018, http://www.noticekorea.com/?p=2725.

[106] F.A. Danevich, V. V. Kobychev, O.A. Ponkratenko, V.I. Tretyak, Y.G.

Zdesenko, Quest for double beta decay of ^{160}Gd and Ce isotopes, Nucl. Phys. A. 694 (2001) 375–391. https://doi.org/10.1016/S0375-9474(01)00983-6.

[107] R.D.Enea, L.Spezia, Chapter 11: Gamma Spectrometry Of Marine Environmental Samples: Problems and Suggestions, 263-270, IAEA (1999). https://inis.iaea.org/collection/NCLCollectionStore/_Public/32/034/32034851.pdf.

[108] F. Arneodo, P. Benetti, A. Bettini, A. Borio Di Tigliole, E. Calligarich, C. Carpanese, *et al*, Calibration of BC501A liquid scintillator cells with monochromatic neutron beams, Nucl. Instr. Met. Phys. Res. Sect. A Accel. Spectrometers, Detect. Assoc. Equip. 418 (1998) 285–299. https://doi.org/10.1016/S0168-9002(98)00679-2.

[109] A. Grau Malonda, E. García-Toraño, J.M. Los Arcos, Liquid-scintillation counting efficiency as a function of the figure of merit for pure beta-particle emitters, Int. J. Appl. Radiat. Isot. 36 (1985) 157–158. https://uwm.edu/safety-health/wp-content/uploads/sites/405/2016/11/handout.pdf.

[110] M.F. L'Annunziata, Handbook of Radioactivity Analysis, Handb. Radioact. Anal. (2003) 1–1273. https://doi.org/10.1016/B978-0-12-436603-9.X5000-5.

[111] J.W. McKlveen, W.J. McDowell, Liquid scintillation alpha spectrometry techniques, Nucl. Instruments Methods Phys. Res. 223 (1984) 372–376. https://doi.org/10.1016/0167-5087(84)90677-X.

[112] M. Yasuoka, Y., Ishii, T., Kataoka, Y., Kubo, T., Suda, H., Tokonami, s., Ishikawa, T., Shinogi, Determination of Radon Concentration in Water Using Liquid Scintillation Counter, Radioisotopes. 53 (2004)

123–131. https://doi.org/10.3769/radioisotopes.53.123.

[113] N. V. Kornilov, I. Fabry, S. Oberstedt, F.J. Hambsch, Total characterization of neutron detectors with a 252Cf source and a new light output determination, Nucl. Instruments Methods Phys. Res. Sect. A Accel. Spectrometers, Detect. Assoc. Equip. 599 (2009) 226–233. https://doi.org/10.1016/j.nima.2008.10.032.

[114] C. William, Light Yield in Liquid Argon for Dark Matter Detection, (2013).

[115] H. Schölermann, H. Klein, Optimizing the energy resolution of scintillation counters at high energies, Nucl. Instruments Methods. 169 (1980) 25–31. https://doi.org/10.1016/0029-554X(80)90097-X.

[116] D. Casadei, Estimating the selection efficiency, J. Instrum. 7 (2012). https://doi.org/10.1088/1748-0221/7/08/P08021.

[117] A. Lintereur, J. Ely, J.Stave, B. Mcdonald, Neutron and Gamma Ray Pulse Shape Discrimination with Polyvinyltoluene, Pacific Northwest National Laboratory Richland, Washington 99352, (2012), https://www.pnnl.gov/main/publications/external/technical_reports/PNNL-21609.pdf

[118] P.Q. Vuong, H.J. Kim, H. Park, G. Rooh, S.H. Kim, Pulse shape discrimination study with Tl_2ZrCl_6 crystal scintillator, Radiat. Meas. 123 (2019) 83–87. https://doi.org/10.1016/j.radmeas.2019.02.007.

[119] Y.R.K. S. J. Noh, H. J. Kim, H. Kim, M. W. Lee, D. H. Jeong, J. K. Kim, S. H. Nam, Kwangmo Yang, Optimization for tritium radioactivity analysis in rain water by liquid scintillation counter, KNS. (2016). https://www.kns.org/files/pre_paper/35/16S-698노성진.pdf.

[120] J. Nikolov, I. Stojković, N. Todorović, B. Tenjović, S. Vuković, J. Knežević, Evaluation of different LSC methods for ^{222}Rn determination

in waters, Appl. Radiat. Isot. 142 (2018) 56–63. https://doi.org/10.1016/j.apradiso.2018.09.013.

[121] S.F. Abdul Sani, M.K. Muhamad Azim, A.A. Marzuki, M.U. Khandaker, K.S. Almugren, E. Daar, F.H. Alkallas, D.A. Bradley, Radioactivity and elemental concentrations of natural and commercial salt, Radiat. Phys. Chem. 190 (2022) 109790. https://doi.org/https://doi.org/10.1016/j.radphyschem.2021.109790.

[122] A.S. Alabood, S. H.Kadhim, A. H.Harjan, A.Q. Ahmed, M.Y.Hadi, Estimation of Radiological Hazards due to Natural Radioactivity in Shampoo Samples Used in Iraqi Markets, J. Phys. Conf. Ser. 1294 (2019). https://doi.org/10.1088/1742-6596/1294/2/022024.

[123] F. Chen, X. Wang, Y. Li, Z. Zhang, Analysis of tritium activity concentrations in urine and internal dose assessment for nuclear power plant workers, Radiat. Med. Prot. 2 (2021) 1–4. https://doi.org/10.1016/j.radmp.2020.12.001.

[124] P.L. Ho, L.D. Hung, V.T. Minh, D. Van Chinh, T.T. Thanh, C. Van Tao, Simultaneous Determination of Gross Alpha/Beta Activities in Groundwater for Ingestion Effective Dose and its Associated Public Health Risk Prevention, Sci. Rep. 10 (2020) 1–10. https://doi.org/10.1038/s41598-020-61203-y.

[125] L.A. Currie, Limits for Qualitative Detection and Quantitative Determination: Application to Radiochemistry, Anal. Chem. 40 (1968) 586–593. https://doi.org/10.1021/ac60259a007.

[126] J.L. Erchinger, C.E. Aalseth, B.E. Bernacki, M. Douglas, E.S. Fuller, M.E. Keillor, S.M. Morley, C.A. Mullen, J.L. Orrell, M.E. Panisko, G.A. Warren, R.O. Williams, M.E. Wright, Development of a low background liquid scintillation counter for a shallow underground

laboratory, Appl. Radiat. Isot. 105 (2015) 209–218. https://doi.org/10.1016/j.apradiso.2015.08.027.

[127] X. Meng, Y. Liu, B. Wu, J. Cheng, L. Wang, Y. Wang, N. Su, Minimum Detectable Activity of Pb-210 in Skull From In vivo Measurements: Insights From the Literature, Front. Energy Res. 9 (2021) 1–9. https://doi.org/10.3389/fenrg.2021.759850.

[128] I. Stojković, N. Todorović, J. Nikolov, I. Krajcar Bronić, J. Barešić, N.S.P.N.Y. Kozmidic Luburić NY, USA, Methodology of tritium determination in aqueous samples by Liquid Scintillation Counting techniques, (2018) 99–156.

[129] W.N. Choi, U.J. Lee, J.W. Bae, H.R. Kim, J. Nikolov, I. Stojković, N. Todorović, B. Tenjović, S. Vuković, J. Knežević, Minimum detectable activity of plastic scintillator for in-situ beta measurement system in ground water, Nucl. Eng. Technol. 142 (2018) 56–63. https://doi.org/10.1016/j.net.2019.02.001.

[130] L.Y. Johansson, Determination of Pb-210 and Po-210 in aqueous environmental samples, Acta Chim. Slov. 48 (2008) 199–213. https://www.nrc.gov/docs/ML1105/ML110560301.pdf.

[131] X.G. Feng, Q.G. He, J.C. Wang, J. Chen, (ANUP2012) expanded applications of liquid scintillation counting and several related issues, Energy Procedia. 39 (2013) 141–150. https://doi.org/10.1016/j.egypro.2013.07.200.

[132] J.S. Cho, J.K. Ahn, H.C. Kim, D.W. Lee, Radon concentrations in groundwater in Busan measured with a liquid scintillation counter method, J. Environ. Radioact. 75 (2004) 105–112. https://doi.org/10.1016/j.jenvrad.2003.06.002.

[133] I. Stojković, N. Todorović, J. Nikolov, B. Tenjović, PSA discriminator

influence on 222Rn efficiency detection in waters by liquid scintillation counting, Appl. Radiat. Isot. 112 (2016) 80–88. https://doi.org/10.1016/j.apradiso.2016.03.020.

[134] T. Kiliari, I. Pashalidis, Determination of aquatic radon by liquid scintillation counting and airborne radon monitoring system, Radiat. Meas. 43 (2008) 1463–1466. https://doi.org/10.1016/j.radmeas.2008.03.006.

[135] R. Tanaka, S. Araki, Y. Yasuoka, T. Mukai, S. Ohnuma, T. Ishikawa, N. Fukuhori, T. Sanada, A Simplified Method for Improved Determination of Radon Concentration in Environmental Water Samples, Radioisotopes. 62 (2013) 423–438. https://doi.org/10.3769/radioisotopes.62.423.

[136] H. Bem, M. Długosz-Lisiecka, S. Janiak, D. Mazurek, P. Szajerski, Fast determination of indoor radon (222Rn) concentration using liquid scintillation counting, J. Radioanal. Nucl. Chem. 312 (2017) 337–342. https://doi.org/10.1007/s10967-017-5226-x.

[137] J.-S. Cho, H.-M. Lee, S.-W. Kim, J. Kim, A Study on the Variation of Rn-222 Concentration in Groundwater at Busan-Geumjeong area, J. Radiat. Prot. Res. 37 (2012) 149–158. https://doi.org/10.14407/jrp.2012.37.3.149.

[138] H. Kim, Y. Jung, W. Lee, G.-S. Choi, K.H. Chung, M.J. Kang, Comparison of the Quantulus 1220 and 300SL Liquid Scintillation Counters for the Analysis of 222 Rn in Groundwater , J. Radiat. Prot. Res. 41 (2016) 395–401. https://doi.org/10.14407/jrpr.2016.41.4.395.

[139] T. Rühle, B. H., Rapid procedure for determining radon-222 in drinking water: H-Rn-222-TWASS-01, Federal coordinating office for drinking water, groundwater, wastewater, sludge, waste and wastewater of

nuclear power plants (1994). https://www.bmuv.de/fileadmin/Daten_BMU/Download_PDF/Strahlenschutz/leitstelle_h_rn_222_twass_01_v1994_12_en.pdf

[140] C. Abesser, Measuring radon in water using a portable liquid scintillation counter, (2009). https://nora.nerc.ac.uk/id/eprint/6763/1/OR09006.pdf.

[141] F.F. Dias, M.H.T. Taddei, Rn-222 Determination in Drinking Water Samples in a Region with Elevated Natural Radioactivity in Brazil : Comparison Between Liquid Scintillation Counting and Gamma Spectrometry, Sci. Commun. - TERRAE. 6, 72-76 (2009). https://www.ige.unicamp.br/terrae/V6/PDF-N6/T-a7i.pdf.

[142] W.E. Potter, J. Strzelczyk, Measurements should not be recorded as less than MDA: An extension, Health Phys. 94 (2008) 62–64. https://doi.org/10.1097/01.HP.0000304156.82787.96.

액체 섬광 계수 시스템을 기반으로 한 새로운 라돈 검출 기술

아모스 빈센트 은타리사

경북대학교 대학원 물리학과 핵물리학전공
(지도교수 김홍주)

(초 록)

라돈은 인간의 건강에 해로운 영향을 미치기 때문에 라돈의 검출과 측정이 점점 중요해지고 있다. 라돈은 흡연에 이어 폐암의 두 번째 주요 원인이며, 일반적으로 평생 담배를 피워본 적이 없는 사람들의 폐암 발생 주요 원인이다. 본 연구에서는 새로운 액체 섬광 기술을 사용하여 3개의 자연 발생 라돈 동위원소(^{222}Rn,^{220}Rn, ^{219}Rn)를 동시에 검출하였다. 사용된 검출 방법은 지연된 일치 기법(the delayed coincidence technique)과 디지털 전하 비교(digital charge comparison)를 사용한 펄스 형상 판별(pulse shape discrimination)이다. 또한 표준 ^{22}Na, ^{60}Co 및 ^{137}Cs 감마 선원을 사용한 몬테카를로 시뮬레이션을 통해 검출기의 감마 응답 함수를 결정한다. 또한 측정된 광 출력 분포와 시뮬레이션을 비교함으로써 검출기 분해능과 에너지 교정 파라미터도 결정하였다. 측정 전 대기 중 라돈 가스를 울티마 골드 AB 700 mL에 48시간 동안 주입하였다. ^{222}Rn(^{238}U),^{220}Rn(^{232}Th)및 ^{219}Rn(^{235}U) 붕괴사슬의 최소 검출가능 방사능(minimum detectable activity)은 각각 1.7, 1.0, 1.2 mBq/L로 결정되었다. 본 연구에서 제안된 새로운 기술은 물 샘플에서 자연적으로 발생하는 세 가지 라돈 동위원소를 모두 식별하는 데 사용될 가능성이 있다.

List of publications

1) **Amos Vincent Ntarisa**, H.J. Kim, Pabitra Aryal, Nguyen Duy Quang, Sudipta Saha, *Novel technique for simultaneous detecting three naturally occurring radon isotopes (^{222}Rn, ^{220}Rn and ^{219}Rn), Radiation Physics and Chemistry*. https://doi.org/10.1016/j.radphyschem.2022.110202

2) **Amos Vincent Ntarisa**, Sudipta Saha, N.D. Quang, H.J. Kim, N. Wantana, I.R. Pandey, P. Aryal, S. Kothan, J. Kaewkhao, *Fabrication and investigation of the effects of various gadolinium compounds on Ce^{3+} - activated phosphate glasses for scintillation applications, Optik, Volume 262, July 2022, 169303. https://doi.org/10.1016/j.ijleo.2022.169303*

3) **Amos Vincent Ntarisa**, Sudipta Saha, P. Aryal, H.J. Kim, A. Khan, N.D. Quang, I.R. Pandey, J. Kaewkhao, S. Kothan, *Luminescence and scintillation properties of Ce^{3+}-doped P_2O_5-Li_2CO_3-$GdBr_3$-Al_2O_3 glasses, J. Non. Cryst. Solids. 567 (2021) 120914*. https://doi.org/10.1016/j.jnoncrysol.2021.120914

4) **Amos Vincent Ntarisa**, D.J. Daniel, D. Balaji, A. Raja, H.J. Kim, N.D. Quang, *A novel blue-emitting phosphors ($CsBaYB_6O_{12}$:Ce^{3+}): Potential applications in w-LEDs and X-ray phosphors, J. Alloys Compd. 873 (2021) 159676.* https://doi.org/10.1016/j.jallcom.2021.159676

5) Sudipta Saha, **Amos Vincent Ntarisa**, N. D. Quang, N. T. Luan, P. Q. Vuong, H. J. Kim, S. Kothan, J. Kaewkhao, *Scintillation performance of the Ce^{3+}-activated lithium phosphate glass, Radiation Physics and Chemistry* https://doi.org/10.1016/j.radphyschem.2022.110285

6) Sudipta Saha, **Amos Vincent Ntarisa**, Nguyen Duy Quang, H.J. Kim, S. Kothan, J. Kaewkhao, *Synthesis and Elemental Analysis of Gadolinium Halides (GdX_3) in Glass Matrix for Radiation Detection Applications, Optical Materials, Volume 129, July 2022, 112490. https://doi.org/10.1016/j.optmat.2022.112490*

7) Yong Seok Hwang, Pabitra Aryal, HongJoo Kim, **Amos vincent Ntarisa**, Sudipta Saha, Chorong Kim, S. Kothan, J. Kaewkhao, *Mn^{2+} Doping*

Inside Glass Substrate Utilizing Metal-Ion Beam Implantation Technique, Optik, Volume 262, July 2022, 169270. https://doi.org/10.1016/j.ijleo.2022.169270

8) Sudipta Saha, H.J.Kim, Arshad Khan, Jaeyoung Cho, Sinchul Kang, **Amos Vincent Ntarisa,** *Synthesis and luminescence studies of* Dy^{3+} *doped* $Li_3Sc(BO_3)_2$ *polycrystalline powder for warm white light, Ceramics International Volume 48, Issue 8, 15 April 2022, Pages 10667-10676,* https://doi.org/10.1016/j.ceramint.2021.12.281

9) P. Aryal, S. Saha, H.J. Kim, S.J. Kang, **Amos Vincent Ntarisa**, A. Angnanon, J. Kaewkhao, *Synthesis and characterization of* CeF_3 *– doped (* $74 . 5\text{-}x$ *)* $P_2O_5 : 20Li_2O : 5Al_2O_3 : x(GdF_3$*,* LaF_3 *and* $YF_3)$ *glasses, Radiation Physics and Chemistry, 109700 189 (2021) 3–8.* https://doi.org/10.1016/j.radphyschem.2021.109700

10) Pabitra Aryal, HongJoo Kim, Sudipta Saha, Jaeyoung Cho, **Amos Vincent Ntarisa**, Suchart Kothan, Jakrapong Kaewkhao, *Rapid and convenient crystallization of quantum dot* $CsPbBr_3$ *inside a phosphate glass matrix, Journal of Alloys and Compounds, 866 (2021), 158974.* https://doi.org/10.1016/j.jallcom.2021.158974

List of conferences presentations

1) **Amos Vincent Ntarisa**, H.J. Kim, Pabitra Aryal, Nguyen Duy Quang, *Developing a novel technique of radon detection for all three naturally occurring radon (^{222}Rn, ^{220}Rn, and ^{219}Rn), 15th International Symposium on Radiation Physics (ISRP-15) December 6 - 10, 2021, Sunway University, Kuala Lumpur,* **Malaysia.**

2) **Amos Vincent Ntarisa**, H.J. Kim, Pabitra Aryal, Nguyen Duy Quang, *A method for detection for all three naturally occurring radon, The LSC2020 conference, Advance in liquid Scintillation Spectrometry, October 18th-20th 0ctober, 2021 - Shenzhen Technology University, Laser Fusion Research Center, - Shenzhen***, China**.

3) **Amos Vincent Ntarisa**, Pabitra Aryal, H.J. Kim, *A Method for Measurement of Radon Activity Concentrations, The 4th International Conference on Applied Physics and Material Applications ICAPMA 2019, 18-20 September 2019, Medan,* **Indonesia.**

4) **Amos Vincent Ntarisa**, S. Saha, N.D. Quang, H.J. Kim, N. Wantana, I.R. Pandey, P. Aryal, S. Kothan, J. Kaewkhao, *Fabrication and study on the effect of varying gadolinium compounds on ce^{3+}-activated phosphate glasses for scintillation applications., The 5th International Conference on Applied Physics and Materials Applications & Applied Magnetism and Ferroelectrics (ICAPMA-JMAG-2021), December 1 - 4, 2021, Pattaya,* **Thailand.**

5) **Amos Vincent Ntarisa**, S. Saha, N.D. Quang, H.J. Kim, I.R. Pandey, J. Kaewkhao, N. Wantana, S. Kothan, *The effect of varying Gd on phosphate-lithium-gadolinium-aluminium-cerium doped glasses for scintillation purposes, The Korean Physical Society (KPS) 2021 KPS Fall Meeting, October 20-22, 2021***, Korea.**

6) **Amos Vincent Ntarisa**, Sudipta Saha, HongJoo Kim, Pabitra Aryal, Arshad Khan, Nguyen Duy Quang, Indra Raj Pandey, Jakrapong Kaewkhao, Suchart Kothan, *Fabrication and study of Ce^{3+} doped phosphate glass for alpha and gamma detection**,** The Korean Physical Society (KPS) 2021 Spring Meeting April 21-23, 202 1,* **Korea.**

7) **Amos Vincent Ntarisa**, D. Joseph Daniel, H.J. Kim, Nguyen Duy Quang, *Synthesis, and luminescence properties of* Ce^{3+} *doped* $CsBaYB_6O_{12}$ *phosphor. The Korean Physical Society (KPS) 2020 KPS Fall Meeting November 4 – 6, 2020,* **Korea**.

8) **Amos Vincent Ntarisa**, Pabitra Aryal, H.J. Kim, *Development of a Technique for the Assessment of Radon Concentration, The Korean Physical Society (KPS) 2020 Spring Meeting July 13 – 15, 2020, Changwon Exhibition Convention Center (CECO), Changwon***, Korea**.

9) **Amos Vincent Ntarisa**, H.J. Kim, Pabitra Aryal, *Sensitivity of the Detection Technique for Determining Radon in Water, The Korean Physical Society (KPS), 2019 KPS Fall Meeting, October 23 – 25, 2019, Kimdaejung Convention Center (KDJ Center, Gwangju*, **Korea**

10) **Amos Vincent Ntarisa**, Pabitra Aryal, H.J. Kim, *Developing Radon Detection Techniques with Liquid Scintillator and Photomultiplier Tube, The Korean Physical Society (KPS) 2018 Fall Meeting, October 24-26, 2018,* Changwon Exhibition Convention Center, Changwon, **Korea**